Closed-form analytical solutions for predicting stress transfers and thermo-elastic properties of short fiber composites

E. Rashidinejad[1,*] , H. Ahmadi[1], M. Hajikazemi[1,2], W. Van Paepegem[1]

[1]*Department of Materials, Textiles and Chemical Engineering, Faculty of Engineering and Architecture, Ghent University, Technologiepark Zwijnaarde 46, Ghent, Belgium*

[2]*Dutch Polymer Institute (DPI), P.O. Box 902, 5600 AX, Eindhoven, The Netherlands*

*Corresponding author: Ehsan.Rashidinejad@ugent.be, Postal address: Technologiepark 46, 9052 Zwijnaarde, Ghent, Belgium.

Closed-form analytical solutions for predicting stress transfers and thermo-elastic properties of short fiber composites

Novel analytical solutions with closed-form expressions for the stress and displacement fields of short fiber reinforced composites (SFRCs) and analytical prediction of their effective thermo-elastic properties are presented. The cylindrical SFRC unit-cells with periodic boundary conditions are subjected to axial and transverse stresses as well as thermally induced residual stresses. By comparison with available numerical and analytical solutions, it is revealed that the present closed-form solutions provide accurate stress field variations as well as accurate predictions for the effective thermo-elastic properties of SFRCs in a split second and thus, the developed model is much more computationally efficient than numerical methods.

Keywords: Short fiber reinforced composites; Analytical modeling; Fiber-matrix stress transfer; Effective thermo-elastic properties; Cylindrical short fiber model; Periodic boundary conditions

1. Introduction

Recently, short fiber reinforced composites (SFRCs) have attracted the attention of a large number of industrial applications. These composites can be mass-produced by fast and cheap processes such as injection molding while they have high strength-to-weight ratios, [1-7]. SFRCs are widely used in different industrial sectors [8-12] as potential replacements for the metallic semi-structural parts, more specifically in automotive industries [13-15]. For engineering and industrial applications, computationally efficient modeling techniques that can accurately estimate the effective thermo-mechanical response of SFRCs are of significant interest.

Mechanical behavior of SFRCs depends on different characteristics of fibers which have been investigated by many researchers from various points of view. The tensile behavior of aligned Glass and Carbon SFRCs was studied by Fu et al. [3] and they described the relationship between the average fiber length and fiber volume fraction. Thomason [16] compared the mechanical properties of injection molded short and long Glass fiber-polypropylene composites with different fiber contents. Bounds on the effective mechanical properties of randomly distributed SFRCs were derived by Rakow and Waas [17]. McCartney [18] investigated the multi-phase composites reinforced with aligned transversely isotropic spheroidal inclusions and demonstrated the effects of fiber volume fraction on the effective properties of composites. Effects of fiber length and volume fraction on thermo-elastic properties of Carbon SFRCs were examined by Karsli and Aytac [19]. Gulrez et al. [20] studied the thermomechanical properties of Carbon SFRCs with various fiber lengths. The effects of fiber length and fiber content on the mechanical properties of short fiber composites were studied by Velumani et al. [21]. By using representative volume elements (RVEs) with periodic boundary conditions (PBCs), Babu et al. [22] predicted the effective mechanical properties of SFRCs with different volume fractions. Shu and

Stanciulescu [23] proposed a multi-scale homogenization approach for predicting the effective elastic properties of SFRCs with various fiber volume fractions and aspect ratios. Effective properties of SFRCs with various geometrical configurations were investigated by Rashidinejad et al. [24] using an enhanced mean-field homogenization and modified Eshelby tensors.

The microstructure of SFRCs results in significant anisotropy in the thermo-mechanical behavior of the composite, [25-28]. The anisotropy effects in SFRCs have been studied by many researchers. Fu and Lauke [29] characterized the anisotropy of the elastic modulus of misaligned SFRCs and subsequently, they studied the effects of anisotropy on the strength of SFRCs [30]. De Monte et al. [31] investigated the anisotropic mechanical properties of Glass SFRCs by examining specimens with different thicknesses and various fiber orientations. Effects of fiber orientations on degree of anisotropy, tensile strength and elastic modulus of SFRCs were also experimentally studied by Mortazavian and Fatemi [32]. Cai et al. [33] analyzed the anisotropic behavior of SFRCs via a microstructure modelling scheme. In addition, fiber alignment as well as orientation distribution have significant effects on the effective behavior of SFRCs which are examined in many researches, see e.g. [32, 34-36].

Different authors have investigated the effective behavior of SFRCs by using various micromechanical models and RVEs. Kari et al. [37] evaluated the effective properties of randomly distributed SFRCs by using a numerical homogenization technique based on FE analysis. Zhao et al. [38] examined the effects of micromechanics model in predicting mechanical properties of SFRCs. By using RVE scheme and FE analysis, Zhong et al. [39] investigated the elastic properties of injection molded SFRCs and their relations with volume fraction, average fiber length and orientation. Some authors have compared various modeling approaches for prediction of the effective properties of SFRCs. Tucker and Liang [40] reviewed and compared the predictions of different modeling techniques for unidirectional SFRCs. Naili et al. [41] compared the effective elastic properties of SFRCs predicted by FE analyses of RVEs and homogenization methods. Among different methodologies for predicting the effective properties of SFRCs, Mean-Field Homogenization (MFH) schemes are attractive approaches that are often used, [40, 42-46]. Recently, Hessman et al. [47] revisited MFH approaches for predicting the effective properties of SFRCs and compared their predictions with numerical homogenization. However, MFHs provide the effective properties of the composite by computing the average stress/strain components in the fibers and matrix, and the realistic stress/strain variations involving stress concentrations at the fiber tips and at the interface between the fiber and matrix cannot be given by MFH methods, see [24, 40]. Among classical analytical schemes, only shear-lag models (firstly introduced by Cox [48] and then modified by some authors such as Clyne [49]) are able to give an estimate for variation of the axial stresses in the short fiber.

The effective properties of SFRCs can be predicted by both “MFH approaches” and “numerical and analytical full-field methods”. While MFHs predict the effective properties of the composite by estimating the average elastic fields,

numerical and analytical full-field methods can evaluate the stress/strain variations as well as the effective properties of SFRCs. Numerical full-field methods such as FE analysis (e.g., [41, 50]) provide accurate predictions for the effective properties of SFRCs and fiber-matrix stress transfers. However, FE approaches are subjected to high calculation costs and therefore are not computationally efficient. Analytical full-field approaches may be more efficient but may also include intricate mathematical manipulations and complications especially when material anisotropy is taken into account (e.g., see [51, 52]). An analytical model for prediction of the elastic fields in SFRCs with isotropic fibers and matrix has been developed by Jiang et al. [53] where simplifying assumptions are made on the radial and circumferential stress components. This analytical model was then extended by Huang et al. [54] for predicting the effective properties of SFRCs with transversely isotropic fibers. Moreover, in analytical solutions complex interactions between the inhomogeneities should be thoroughly incorporated which add more difficulty to analytical treatments, see [55-57]. Therefore, an accurate and efficient closed-form analytical solution for the fiber-matrix stress transfers and effective thermo-elastic properties of SFRCs would be of great importance for predicting the response of SFRCs in their engineering applications under various loading conditions.

The purpose of this paper is to develop an efficient analytical model for accurate determination of the elastic fields and stress transfers in SFRCs and subsequently prediction of their effective thermo-elastic properties in both the axial and transverse directions. To this end, the topic is divided into two main steps. In the first step, a cylindrical anisotropic short fiber unit-cell subjected to PBCs is investigated. To develop closed-form solutions for the short fiber unit-cells, the analytical treatments of Nairn [58] and McCartney [59] which were developed for continuous fiber systems are rigorously extended to the short fiber systems. Moreover, the effects of PBCs are also implemented in the cylindrical short fiber model. By solving the required equilibrium and constitutive equations, novel closed-form solutions for the elastic stress/displacement fields in the cylindrical short fiber model are developed. In the second step, the developed analytical solutions are utilized for determination of the effective axial and transverse thermo-elastic properties of SFRCs. For this purpose, the short fiber unit-cell is subjected to different axial, transverse and thermal loading conditions and the axial and transverse shear moduli are estimated by using the Maxwell approach [18] assuming uniform shear strains along the short fiber unit-cell. For demonstration of the efficiency and capabilities of the developed analytical model, the effective thermo-elastic properties of various Glass and Carbon SFRCs with different volume fractions and aspect ratios are predicted, compared and validated with available analytical and FE numerical data in the literature. Furthermore, the stress variations obtained from the present closed-form solutions are compared with available FE numerical data in the literature where very good agreement is observed. It should be noted that the present study is mainly concerned with accurate prediction of the local elastic fields and effective thermo-elastic properties of unidirectional SFRCs. However, for obtaining the effective properties of misaligned SFRCs, as described by Advani and Tucker [60] and Dray et al. [35]

orientation distribution of the fibers and the corresponding orientation tensor can be applied to the stiffness tensor of aligned SFRC evaluated by the current analytical development.

The present paper is organized as follows. In Section 2, the cylindrical short fiber model with PBCs is described and the corresponding equilibrium, compatibility and constitutive equations as well as the general solution of the problem are presented. The analytical closed-form solutions for the stress and displacement fields in the cylindrical short fiber model are developed in Section 3. By using the interfacial boundary conditions, the stress transfer functions are derived explicitly in Section 4. Subsequently, in Section 5 the developed analytical solutions are utilized for determination of the effective axial and transverse thermo-elastic properties of SFRCs. Section 6 is focused on evaluation of the stress fields and effective thermo-elastic properties of various Glass and Carbon SFRCs where predictions of the developed model are compared and validated with analytical and numerical data available in the literature. Finally, concluding remarks are presented in Section 7.

2. Geometry, basic field equations and boundary conditions

In this section, a transversely isotropic cylindrical short fiber embedded in an isotropic cylindrical matrix is considered and the corresponding field equations and boundary conditions are explained. The cylindrical short fiber model is subjected to periodic boundary conditions (PBCs) in the axial direction and uniform circumferential radial displacement representing periodic-like boundary conditions (PLBCs) in the transverse direction (Figs. 1(a)-(c)). The transversely isotropic short fiber with axial Young's modulus E_A^f, transverse Young's modulus E_T^f, axial Poisson's ratio ν_A^f, transverse Poisson's ratio ν_T^f, axial shear modulus μ_A^f, and transverse shear modulus $\mu_T^f = E_T^f/(2+2\nu_T^f)$ is surrounded by isotropic matrix with Young's modulus E^m, Poisson's ratio ν^m, and shear modulus $\mu^m = E^m/(2+2\nu^m)$. The axial and transverse thermal expansion coefficients for the fiber are denoted by α_A^f and α_T^f while the thermal expansion coefficient of the isotropic matrix is α^m. The cylindrical short fiber with length $2L$ and radius R is embedded in the cylindrical matrix with length $2(L+w)$ and radius $a > R$ as shown in Fig. 1(b). The aspect ratio of the cylindrical short fiber is then L/R. The axisymmetric cylindrical system is subjected to an average axial stress σ_A, an average transverse stress σ_T applied upon the external surface of the cylindrical matrix, and a uniform temperature change ΔT. It should be noted that the tip-to-tip interactions of the short fibers are taken into account by consideration of their tip distance ($w_{\text{tip}} = 2w$) through their periodic distribution in the axial direction (see Fig. 1(a)). The origin of the cylindrical coordinate system is set at the center-point of the short fiber with the z-axis lying along the common axis of the concentric cylinders (Fig. 1(c)) so that the axisymmetric cylindrical ensemble also has reflection symmetry with respect to the plane $z = 0$. Therefore, the problem under consideration is solved in the assumed cylindrical coordinates with $0 \le r \le a$ and $0 \le z \le L + w$.

Fig. 1

In the concentric cylindrical short fiber model shown in Fig. 1, the fictitious longitudinal extension of the fiber into the matrix is named as the "fiber-image" lying within $0 \le r \le R$ and $L \le z \le L + w$ (see Fig. 1(c)). The reason for introducing the fiber-image region is that although the material properties of the fiber-image and its surrounding matrix are identical, variations of the stress and displacement components within the fiber-image are basically different from those in the matrix. In the next section, the solutions associated with the fiber-image and its surrounding matrix are identified and discussed in details. As shown in Fig. 1(d), the fiber and fiber-image cross-sectional area is $S_f = R^2/a^2$ while the matrix cross-sectional area is $S_m = (a^2 - R^2)/a^2 = 1 - S_f$. It is then clear that the volume fraction of the short fiber (v_f) is related to the fiber area by $v_f = S_f L/(L + w)$. For the axisymmetric problem under consideration, the equilibrium equations reduce to

$$\frac{\partial \sigma_{rr}}{\partial r} + \frac{\partial \sigma_{rz}}{\partial z} + \frac{\sigma_{rr} - \sigma_{\theta\theta}}{r} = 0, \tag{1}$$

$$\frac{\partial \sigma_{rz}}{\partial r} + \frac{\partial \sigma_{zz}}{\partial z} + \frac{\sigma_{rz}}{r} = 0. \tag{2}$$

The constitutive equations corresponding to an axisymmetric transversely isotropic medium are written in the form

$$\frac{\partial u_r}{\partial r} = \epsilon_{rr} = \frac{1}{E_T}\sigma_{rr} - \frac{\nu_T}{E_T}\sigma_{\theta\theta} - \frac{\nu_A}{E_A}\sigma_{zz} + \alpha_T \Delta T, \tag{3}$$

$$\frac{u_r}{r} = \epsilon_{\theta\theta} = \frac{1}{E_T}\sigma_{\theta\theta} - \frac{\nu_T}{E_T}\sigma_{rr} - \frac{\nu_A}{E_A}\sigma_{zz} + \alpha_T \Delta T, \tag{4}$$

$$\frac{\partial u_z}{\partial z} = \epsilon_{zz} = \frac{1}{E_A}\sigma_{zz} - \frac{\nu_A}{E_A}\sigma_{rr} - \frac{\nu_A}{E_A}\sigma_{\theta\theta} + \alpha_A \Delta T, \tag{5}$$

$$\frac{1}{2}\left(\frac{\partial u_r}{\partial z} + \frac{\partial u_z}{\partial r}\right) = \epsilon_{rz} = \frac{1}{2\mu_A}\sigma_{rz}, \tag{6}$$

in which E, ν, μ and α are the Young's modulus, Poisson's ratios, shear modulus and thermal expansion coefficient, respectively, and subscripts A and T represent for the axial and transverse directions. When the axial stress σ_{zz} as well as the temperature change ΔT are independent of the radial coordinate r, the compatibility condition can be written as (see [58, 59])

$$(1 + \nu_T)\frac{\sigma_{rr} - \sigma_{\theta\theta}}{r} = \frac{\partial}{\partial r}(\sigma_{\theta\theta} - \nu_T \sigma_{rr}). \tag{7}$$

In the remainder of this section, superscripts f or m over a field component indicate that the component corresponds to the fiber and fiber-image ($0 \le r \le R$) or the matrix ($R \le r \le a$), respectively. Therefore, the interfacial boundary conditions of the concentric fiber-matrix cylindrical system that must be satisfied are written as follows:

$$\sigma_{rr}^f(R, z) = \sigma_{rr}^m(R, z), \tag{8}$$

$$\sigma_{rz}^f(R, z) = \sigma_{rz}^m(R, z), \tag{9}$$

$$u_r^f(R, z) = u_r^m(R, z), \tag{10}$$

$$u_z^f(R,z) = u_z^m(R,z), \tag{11}$$

where $0 \le z \le L + w$. Moreover, on the external surface of the short fiber cylindrical system the following boundary conditions are imposed:

$$\sigma_{rz}^m(a,z) = 0, \quad 0 \le z \le L + w, \tag{12}$$

$$\frac{1}{L+w}\int_0^{L+w} \sigma_{rr}^m(a,z)\, dz = \sigma_T, \tag{13}$$

while in the axial direction, the following condition holds at any point z:

$$S_f \sigma_{zz}^f(z) + S_m \sigma_{zz}^m(z) = \sigma_A, \quad 0 \le z \le L + w. \tag{14}$$

Symmetry of the problem with respect to $z = 0$ in addition to PBCs in the axial direction require that the cylindrical fiber-matrix unit-cell undergoes uniform axial displacement at $z = \pm(L + w)$. In order to implement PLBCs for the transverse direction in the axisymmetric cylindrical model, the following boundary condition is imposed implying a uniform radial displacement on the external surface of the outer cylinder along the whole length of the cylindrical ensemble (see Fig. 1(c)):

$$u_r^m(a,z) = U_0, \quad 0 \le z \le L + w, \tag{15}$$

where U_0 is an unknown uniform radial displacement to be obtained for any given average axial stress σ_A, average transverse stress σ_T and temperature change ΔT.

The boundary conditions on the continuity of the interfacial traction stress components at the fiber tip ($z = L$) are written as

$$\sigma_{zz}^f(L^-) = \sigma_{zz}^f(L^+), \tag{16}$$

$$\sigma_{zz}^m(L^-) = \sigma_{zz}^m(L^+), \tag{17}$$

$$\sigma_{rz}^f(r,L^-) = \sigma_{rz}^f(r,L^+), \tag{18}$$

$$\sigma_{rz}^m(r,L^-) = \sigma_{rz}^m(r,L^+), \tag{19}$$

while continuity of the displacement components at the interface $z = L$ are expressed as

$$u_z^f(r,L^-) = u_z^f(r,L^+), \tag{20}$$

$$u_z^m(r,L^-) = u_z^m(r,L^+), \tag{21}$$

$$u_r^f(r,L^-) = u_r^f(r,L^+), \tag{22}$$

$$u_r^m(r,L^-) = u_r^m(r,L^+). \tag{23}$$

In the above boundary conditions, the signs $-$ or $+$ over the coordinate L indicate that the point is located at the left or right side of the interface $z = L$, respectively.

For the considered axisymmetric system, the general solution for non-zero stress components in the cylindrical fiber or fiber-image and the cylindrical matrix can be expressed in terms of the stress transfer function $C(z)$ and unknown functions $R_f(z)$, $R_m(z)$, and $Y_m(z)$ as follows (see [58, 59]):

$$\sigma_{zz}^{f}(z) = \sigma_f - C(z), \tag{24}$$

$$\sigma_{rz}^{f}(r,z) = \frac{r}{2}C'(z), \tag{25}$$

$$\sigma_{rr}^{f}(r,z) = -\frac{1}{16}\left(3+\nu_T^f\right)C''(z)\,r^2 + R_f(z) + \sigma_{TC} - S_m\frac{\phi}{R^2}, \tag{26}$$

$$\sigma_{\theta\theta}^{f}(r,z) = -\frac{1}{16}\left(1+3\nu_T^f\right)C''(z)\,r^2 + R_f(z) + \sigma_{TC} - S_m\frac{\phi}{R^2}, \tag{27}$$

$$\sigma_{zz}^{m}(z) = \sigma_m + \frac{S_f}{S_m}C(z), \tag{28}$$

$$\sigma_{rz}^{m}(r,z) = \frac{1}{2S_m}C'(z)\left(\frac{R^2}{r} - S_f\,r\right), \tag{29}$$

$$\sigma_{rr}^{m}(r,z) = \left\{(3+\nu^m)\frac{r^2}{a^2} - 4(1+\nu^m)\mathrm{Log}\left[\frac{r}{a}\right] - 2(1-\nu^m)\right\}\frac{R^2}{16\ m}C''(z)$$
$$+R_m(z) - \frac{Y_m(z)}{r^2} + \sigma_{TC} + \phi\left(\frac{1}{a^2} - \frac{1}{r^2}\right), \tag{30}$$

$$\sigma_{\theta\theta}^{m}(r,z) = \left\{(1+3\nu^m)\frac{r^2}{a^2} - 4(1+\nu^m)\mathrm{Log}\left[\frac{r}{a}\right] + 2(1-\nu^m)\right\}\frac{R^2}{16S_m}C''(z)$$
$$+R_m(z) + \frac{Y_m(z)}{r^2} + \sigma_{TC} + \phi\left(\frac{1}{a^2} + \frac{1}{r^2}\right), \tag{31}$$

in which the parameters σ_f, σ_m, σ_{TC} and ϕ correspond to the concentric continuous fiber-matrix cylindrical system given in Appendix A. In the above expressions, the boundary conditions (9) and (12) are already satisfied. It is worth noting that for the case of continuous fiber-matrix cylindrical system ($w = 0$), the functions $C(z)$, $R_f(z)$, $R_m(z)$, and $Y_m(z)$ vanish and therefore the solution reduces to the classical solution of concentric continuous fiber-matrix cylinders (as given in Appendix A).

Subsequently, by substituting the above stress components into the constitutive equations (3), (4) and (6) for both fiber/fiber-image ($0 \le r \le R$) and matrix ($R \le r \le a$), the non-zero displacement components associated with the fiber/fiber-image and matrix can be expressed as (see [59])

$$u_r^f(r,z) = -\frac{1-\nu_T^f}{32\mu_T^f}r^3C''(z) + \frac{\nu_A^f}{E_A^f}rC(z) + \frac{1-\nu_T^f}{E_T^f}rR_f(z) + A_f r, \tag{32}$$

$$u_z^f(r,z) = -\frac{1}{2}\left\{\left(\frac{\nu_A^f}{E_A^f} - \frac{1}{2\mu_A^f}\right)C'(z) + \frac{1-\nu_T^f}{E_T^f}R_f'(z)\right\}(r^2-R^2) + \frac{1-\nu_T^f}{128\mu_T^f}C'''(z)(r^4-R^4) + H_f(z) + \epsilon_A z, \tag{33}$$

$$u_r^m(r,z) = \left(\frac{1}{2}\frac{r^3}{a^2} - 2r\mathrm{Log}\left[\frac{r}{a}\right] + r\right)\frac{1-\nu^m}{16\mu^m}\frac{R^2}{S_m}C''(z) - \frac{\nu^m S_f}{E^m S_m}rC(z) + \frac{1-\nu^m}{E^m}rR_m(z) + \frac{Y_m(z)}{2\mu^m r} + A_m r + \frac{\phi}{2\mu^m r}, \tag{34}$$

$$u_z^m(r,z) = -\frac{1}{2}\left\{\frac{S_f}{E^m S_m}C'(z) + \frac{(1-\nu^m)(2-\mathrm{Log}[S_f])}{16\mu^m S_m}R^2C'''(z) + \frac{1-\nu^m}{E^m}R_m'(z)\right\}(r^2-R^2) - \frac{(1-\nu^m)S_f}{128\mu^m S_m}C'''(z)(r^4-R^4)$$
$$+\frac{(1-\nu^m)R^2}{16\ {}^m S_m}C'''(z)r^2\mathrm{Log}\left[\frac{r}{R}\right] + \left(\frac{R^2}{2\mu^m S_m}C'(z) - \frac{Y_m'(z)}{2\mu^m}\right)\mathrm{Log}\left[\frac{r}{R}\right] + H_m(z) + \epsilon_A z, \tag{35}$$

in which A_f and A_m correspond to the displacements in the concentric continuous fiber-matrix cylindrical system given in Appendix A, and $H_f(z)$ and $H_m(z)$ are unknown functions of the axial coordinate to be determined. It should be noted that in Eqs. (24)-(35) a field component with the superscript f corresponds to both the fiber and fiber-image ($0 \le r \le R$). It can be shown that satisfying the boundary condition (11) yields $H_f(z) = H_m(z)$. In the above expressions associated with the stress components (Eqs. (24)-(31)) and displacement components (Eqs. (32)-(35)) in the fiber/fiber-image and the matrix, the only simplifying assumption is that the axial stress σ_{zz} in both the fiber/fiber-image and matrix is assumed to be a function of the axial coordinate only. Eqs. (24)-(31) represent the solutions of the equilibrium equations (1) and (2) and the compatibility equation (7) for a cylindrical fiber-matrix system which were introduced by Nairn [58] and McCartney [59]. Furthermore, in Eqs. (24)-(35) the boundary conditions (9), (11) and (12) as well as the stress-strain constitutive equations (3), (4) and (6) are satisfied exactly. For further details on derivation of Eqs. (24)-(35) by satisfying the equilibrium, compatibility, and constitutive equations together with the boundary conditions, the reader is referred to Refs. [58, 59].

3. Analytical closed-form solutions of the cylindrical short fiber model

In this section, analytical closed-form solutions for the elastic fields of the cylindrical short fiber model under consideration are developed. In order to solve the problem, the cylindrical short fiber unit-cell with $0 \le z \le L + w$ (Fig. 1(c)) is split into two parts, namely "part (I)" and "part (II)" (Fig. 2). Part (I) (with $0 \le z \le L$) is the main portion of the cylindrical model which includes the short fiber. Part (II) (with $L \le z \le L + w$ or equivalently $0 \le z' \le w$) is the remainder of the cylindrical model which consists of only the matrix material, but includes the fiber-image domain with a different solution than the surrounding matrix domain.

Fig. 2

For achieving a complete and accurate solution, the normal and shear stresses transferred between parts (I) and (II) across their interface ($z = L$ or equivalently $z' = w$) should be taken into account. The closed-form solutions of parts (I) and (II) are developed in this section. It should be noted that in the following analytical formulations, superscripts (I) or (II) over a quantity indicate that the quantity corresponds to part (I) or part (II), respectively, while superscripts f, fi or m over a field component indicate that the component corresponds to the fiber, the fiber-image, or the matrix, respectively. Moreover, in the following formulations for convenience the stress transfer function of part (I) is denoted by $C(z)$ while the stress transfer function corresponding to part (II) is denoted by $D(z')$. The stress and displacement representations (24)-(35) are used in both part (I) (with $0 \le z \le L$) and part (II) (with $0 \le z' \le w$), noting that the material constants of

the fiber-image and matrix in part (II) are identical. The boundary conditions (8), (10) and (15) as well as the constitutive relation (5) will also be satisfied in both parts (I) and (II) separately.

For obtaining the solution for part (I), first the unknown functions $R_f^{(I)}(z)$, $R_m^{(I)}(z)$, and $Y_m^{(I)}(z)$ should be determined. By substituting the radial displacement component (Eq. (34)) into the boundary condition (15), the unknown function $Y_m^{(I)}(z)$ can be obtained as:

$$Y_m^{(I)}(z) = a^2\left(\frac{3(\nu^m-1)R^2}{16S_m}C''(z) + \frac{\nu^m S_f}{(1+\nu^m)S_m}C(z) - \frac{1-\nu^m}{1+\nu^m}R_m^{(I)}(z) - 2\mu^m A_m^{(I)}\right) - \phi^{(I)} + 2\mu^m a\, U_0, \tag{36}$$

Substitution of the radial stress components $\sigma_{rr}^{(I),f}$ and $\sigma_{rr}^{(I),m}$ from Eqs. (26) and (30) into the boundary condition (8) and then making use of Eq. (36) result in the following relation between the unknown functions $R_f^{(I)}(z)$ and $R_m^{(I)}(z)$:

$$R_f^{(I)}(z) - \left(1 + \frac{1-\nu^m}{(1+\nu^m)S_f}\right)R_m^{(I)}(z) = L_1(z), \tag{37}$$

where $L_1(z)$ is derived explicitly in terms of the fiber/matrix material and geometrical properties and expressed in Appendix B. By substituting the radial displacement components $u_r^{(I),f}$ and $u_r^{(I),m}$ from Eqs. (32) and (34) into the displacement continuity condition (10) and making use of Eq. (36), another relation between the unknown functions $R_f^{(I)}(z)$ and $R_m^{(I)}(z)$ can be obtained as follows:

$$\frac{1-\nu_T^f}{E_T^f}R_f^{(I)}(z) + \frac{(1-\nu^m)S_m}{E^m S_f}R_m^{(I)}(z) = L_2(z), \tag{38}$$

where $L_2(z)$ is also derived and expressed explicitly in Appendix B. Subsequently, by simultaneous solution of Eqs. (37) and (38) the unknown functions $R_f^{(I)}(z)$ and $R_m^{(I)}(z)$ can be derived analytically in terms of the stress transfer function of part (I) ($C(z)$) and radial displacement U_0 as given in Appendix B. Therefore, the other unknown function $Y_m^{(I)}(z)$ can be obtained by substituting Eq. (B.4) into Eq. (36).

For determination of the stress transfer function $C(z)$ and the other unknown function $H_f(z) = H_m(z)$, the constitutive equation (5) should be satisfied for both fiber and matrix regions. For the stress and displacement representations in Eqs. (24)-(35), it is not possible to satisfy exactly the constitutive equation (5) in the fiber and matrix (see Ref. [59]). However, Eq. (5) can be satisfied in both fiber and matrix regions in the average sense as follows. The constitutive equation (5) is expressed in the following average forms in the fiber and matrix regions, respectively:

$$\frac{d}{dz}\bar{u}_z^{(I),f} = \frac{1}{E_A^f}\bar{\sigma}_{zz}^{(I),f} - \frac{\nu_A^f}{E_A^f}\left(\bar{\sigma}_{rr}^{(I),f} + \bar{\sigma}_{\theta\theta}^{(I),f}\right) + \alpha_A^f \Delta T, \tag{39}$$

$$\frac{d}{dz}\bar{u}_z^{(I),m} = \frac{1}{E^m}\bar{\sigma}_{zz}^{(I),m} - \frac{\nu^m}{E^m}\left(\bar{\sigma}_{rr}^{(I),m} + \bar{\sigma}_{\theta\theta}^{(I),m}\right) + \alpha^m \Delta T, \tag{40}$$

where the overbar over a quantity indicates the average value of the quantity in radial direction over the corresponding cross-section. For any arbitrary functions $\varphi^f(r,z)$ and $\psi^m(r,z)$ associated with the fiber and matrix, respectively, the corresponding average values over the fiber and matrix regions are defined by

$$\bar{\varphi}^f(z) = \frac{1}{\pi R^2}\int_0^R 2\pi r\, \varphi^f(r,z)\, dr, \tag{41}$$

$$\bar{\psi}^m(z) = \frac{1}{\pi(a^2-R^2)}\int_R^a 2\pi r\, \psi^m(r,z)\, dr. \tag{42}$$

By substitution of Eqs. (24), (26), (27) and (33) into Eq. (39) followed by some manipulations, the unknown functions $H_f^{(I)}(z) = H_m^{(I)}(z)$ can be obtained as shown in Appendix B. By using Eqs. (41) and (42) for the average quantities in the fiber and matrix, Eqs. (24), (26), (27) and (33) are then substituted into Eq. (39), and Eqs. (28), (30), (31) and (35) are substituted into Eq. (40). Subsequently, by making use of Eqs. (36), (B.3) and (B.4) followed by a subtraction for eliminating the functions $\frac{d}{dz}H_f^{(I)}(z) = \frac{d}{dz}H_m^{(I)}(z)$, after some manipulations it can be shown that the following non-homogeneous fourth-order differential equation for the stress transfer function $C(z)$ in part (I) holds:

$$F^{(I)}R^4C''''(z) + G^{(I)}R^2C''(z) + H^{(I)}C(z) + K^{(I)} = 0, \quad 0 \le z \le L, \tag{43}$$

in which the coefficients $F^{(I)}$, $G^{(I)}$, $H^{(I)}$, and $K^{(I)}$ are derived as given in Appendix B. By solving the governing differential equation (43), the stress transfer function $C(z)$ can be derived and subsequently, the functions $H_f^{(I)}(z) = H_m^{(I)}(z)$ are determined through Eq. (B.7). By defining the coefficients $r_1 = -G^{(I)}/2F^{(I)}$ and $s_1 = (H^{(I)}/F^{(I)})^{1/2}$ and subsequently $p_1 = \big((r_1+s_1)/2\big)^{1/2}$ and $q_1 = \big((r_1-s_1)/2\big)^{1/2}$, the solution of the governing differential equation (43) can be expressed as

$$C(z) = A_1\mathrm{Cosh}\left[\frac{(p_1+q_1)z}{R}\right] + B_1\mathrm{Cosh}\left[\frac{(p_1-q_1)z}{R}\right] - \frac{K^{(I)}}{H^{(I)}}, \quad 0 \le z \le L, \tag{44}$$

if the value of r_1 is larger than s_1 which is the case for frequent fiber/matrix composites with volume fractions that are not too large (e.g., less than 50%). It has been shown in [59] that a similar situation happens in the case of continuous fiber composite with fiber break under uniform transverse stress. It is worth noting that for the case where r_1 is smaller than s_1, the parameter q_1 is imaginary and therefore, the solution of equation (43) for the stress transfer function can be expressed in the following form:

$$C(z) = A_1\mathrm{Cosh}\left[\frac{p_1 z}{R}\right]\mathrm{Cos}\left[\frac{|q_1|z}{R}\right] + B_1\mathrm{Sinh}\left[\frac{p_1 z}{R}\right]\mathrm{Sin}\left[\frac{|q_1|z}{R}\right] - \frac{K^{(I)}}{H^{(I)}}, \quad 0 \le z \le L. \tag{45}$$

Since we aim to analyze practical SFRCs with not too large volume fractions, the solution (44) is therefore selected as the frequent practical solution of part (I) for such composites. The unknown coefficients A_1 and B_1 are then determined explicitly in Section 4 where the boundary conditions on the normal and shear stresses at the interface of parts (I) and (II) are applied to the developed analytical solutions.

Next, the concentric cylindrical system of part (II) with $0 \le z' \le w$ is considered (see Fig. 2) which consists of the so-called fiber-image ($0 \le r \le R$) surrounded by the matrix ($R \le r \le a$). Although the material properties of the fiber-image and the surrounding matrix are identical, variations of the stress and displacement components within the fiber-image are supposed to be different from those of the matrix. Solution of this part is established in a similar manner as

that of part (I), but with respect to the coordinate z'. Closed-form expressions for the derived functions associated with the solution of part (II) are given in Appendix C. Eqs. (39) and (40) are then rewritten for part (II) while Eqs. (41) and (42) are used for evaluation of the average stress and displacement components corresponding to part (II). Subsequently, by making use of Eqs. (C.1)-(C.3) followed by a subtraction for eliminating the functions $\frac{d}{dz'}H_f^{(II)}(z') = \frac{d}{dz'}H_m^{(II)}(z')$, the following homogeneous fourth-order differential equation for the stress transfer function $D(z')$ in part (II) is obtained:

$$F^{(II)}R^4D''''(z') + G^{(II)}R^2D''(z') + H^{(II)}D(z') = 0, \quad 0 \le z' \le w, \tag{46}$$

in which the coefficients $F^{(II)}$, $G^{(II)}$ and $H^{(II)}$ are derived and expressed in Appendix C. By defining the coefficients $r_2 = -G^{(II)}/2F^{(II)}$ and $s_2 = (H^{(II)}/F^{(II)})^{1/2}$, it can be shown that we always have $r_2 < s_2$. Subsequently, by using $p_2 = \left((r_2 + s_2)/2\right)^{1/2}$ and $q_2 = \left((r_2 - s_2)/2\right)^{1/2}$ and noting that q_2 is imaginary, the solution of the governing differential equation (46) can be expressed as

$$D(z') = A_2\text{Cosh}\left[\frac{p_2z'}{R}\right]\text{Cos}\left[\frac{|q_2|z'}{R}\right] + B_2\text{Sinh}\left[\frac{p_2z'}{R}\right]\text{Sin}\left[\frac{|q_2|z'}{R}\right], \quad 0 \le z' \le w. \tag{47}$$

The unknown coefficients A_2 and B_2 are determined explicitly in Section 4 where the required boundary conditions at the interface of parts (I) and (II) are applied to the developed analytical solution.

It is worth mentioning that the obtained stress/displacement fields for parts I and II exactly satisfy the local stress equilibrium, stress/displacement continuity conditions in the radial and axial directions and balance the applied loads using only one fundamental assumption that the axial stresses in the fiber and matrix are functions of the axial coordinate only. Moreover, the obtained stress and displacement fields satisfy the strain-stress-displacement equations exactly except the one relating axial strain/displacement to stress components (Eq. (5)) which is satisfied in an average sense through the radial direction for the fiber and matrix parts. It was shown in [59] that the resulting stress/displacement fields can accurately minimize the complementary energy functional (see [58]) leading to the optimal solution that can be obtained based on the single fundamental assumption that the axial stresses in the fiber and matrix are independent of the radial coordinate. To find the unique solution, one first needs to determine the constants A_1, B_1, A_2 and B_2 in terms of U_0 by applying appropriate boundary conditions. It should be noted that U_0 is the unknown circumferential displacement in radial direction that has appeared due to considering a uniform radial displacement on the external surface of the cylindrical model along the whole length of both parts (I) and (II). The final unique solution will be obtained by determination of U_0 as will be shown in the next section.

4. Interfacial boundary conditions of parts (I) and (II)

In this section, the traction stress and displacement continuity conditions at the interface between parts (I) and (II) (at $z = L$ and $z' = w$) are applied to the developed analytical solutions. To this end, the boundary conditions (16)-(19) on

the normal and shear stresses transferred across the interface between parts (I) and (II) are utilized in this section for determination of the unknown coefficients in the stress transfer functions of parts (I) and (II). In order to complete the solution, the displacement continuity conditions at the interface of parts (I) and (II) as well as the boundary condition (13) for the average transverse stress at the external surface ($r = a$) of the cylindrical system are then rewritten and satisfied. These boundary conditions are utilized for determination of the normal and shear stresses transferred across the interface of parts (I) and (II) as well as the unknown circumferential radial displacement (U_0).

For determination of the unknown coefficients A_1 and B_1 in the stress transfer function of part (I) given by Eq. (44), the following boundary conditions on the normal and shear stresses at the edge $z = L$ (interface of parts (I) and (II)) are utilized (see Fig. 2):

$$\sigma_{zz}^{(I),f}(L) = \sigma_f^{(I)} - C(L) = \sigma_f^{(I;II)}, \tag{48}$$

$$\sigma_{rz}^{(I),f}(r, L) = \frac{r}{2} C'(L) = \frac{\tau_0}{R} r, \tag{49}$$

where the unknown average normal stress $\sigma_f^{(I;II)}$ occurring at $0 \le r \le R$ and maximum shear stress τ_0 occurring at the point $r = R$ represent the traction stresses at the edge $z = L$ transferred between part (I) and part (II). Recall that $\sigma_f^{(I)}$ is the fiber stress in the concentric continuous fiber-matrix cylindrical system given in Appendix A. By applying the above boundary conditions, the constants A_1 and B_1 in Eq. (44) can be obtained as

$$A_1 = -\Lambda \frac{(p_1 - q_1)\mathrm{Tanh}\left[\frac{(p_1 - q_1)L}{R}\right]}{\mathrm{Cosh}\left[\frac{(p_1 + q_1)L}{R}\right]} \mathcal{F}\left(\sigma_A, \sigma_{TC}^{(I)}, \Delta T, \sigma_f^{(I;II)}, \tau_0, U_0\right), \tag{50}$$

$$B_1 = \Lambda \frac{(p_1 + q_1)\mathrm{Tanh}\left[\frac{(p_1 + q_1)L}{R}\right]}{\mathrm{Cosh}\left[\frac{(p_1 - q_1)L}{R}\right]} \mathcal{F}\left(\sigma_A, \sigma_{TC}^{(I)}, \Delta T, \sigma_f^{(I;II)}, \tau_0, U_0\right) + \frac{2\,\tau_0}{(p_1 - q_1)\mathrm{Sinh}\left[\frac{(p_1 - q_1)L}{R}\right]}, \tag{51}$$

where

$$\Lambda = \frac{1}{(p_1 + q_1)\mathrm{Tanh}\left[\frac{(p_1 + q_1)L}{R}\right] - (p_1 - q_1)\mathrm{Tanh}\left[\frac{(p_1 - q_1)L}{R}\right]}, \tag{52}$$

$$\mathcal{F}\left(\sigma_A, \sigma_{TC}^{(I)}, \Delta T, \sigma_f^{(I;II)}, \tau_0, U_0\right) = \sigma_f^{(I)} - \sigma_f^{(I;II)} + \frac{K^{(I)}}{H^{(I)}} - \frac{2\,\tau_0}{(p_1 - q_1)\mathrm{Tanh}\left[\frac{(p_1 - q_1)L}{R}\right]}. \tag{53}$$

It can be observed that the effects of axial/transverse applied loadings as well as the thermal loading are also captured by the derived solution for the stress transfer function $C(z)$.

For determination of the unknown coefficients A_2 and B_2 in the stress transfer function of part (II), the following boundary conditions on the continuity of normal and shear traction stresses at the edge $z' = w$ are applied to Eq. (47) (see Fig. 2 and Eqs. (48) and (49)):

$$\sigma_{z'z'}^{(II),fi}(w) = \sigma_A - D(w) = \sigma_f^{(I;II)}, \tag{54}$$

$$\sigma_{rz'}^{(II),fi}(r, w) = \frac{r}{2} D'(w) = \frac{-\tau_0}{R} r, \tag{55}$$

noting that in part (II) we have $\sigma_{fi}^{(II)} = \sigma_m^{(II)} = \sigma_A$ ($\sigma_{fi}^{(II)}$ and $\sigma_m^{(II)}$ are the fiber-image and matrix axial stresses in the corresponding continuous cylindrical system given in Appendix A). Moreover, the shear stress in Eq. (55) has a negative sign compared to Eq. (49) since the coordinates z' and z are in inverse directions. By applying the above boundary conditions, the constants A_2 and B_2 in the stress transfer function given by Eq. (47) can be obtained as

$$A_2 = \frac{2\left(p_2\mathrm{Cosh}\left[\frac{p_2 w}{R}\right]\mathrm{Sin}\left[\frac{|q_2|w}{R}\right]+q_2\mathrm{Sinh}\left[\frac{p_2 w}{R}\right]\mathrm{Cos}\left[\frac{|q_2|w}{R}\right]\right)}{p_2\mathrm{Sin}\left[\frac{2|q_2|w}{R}\right]+q_2\mathrm{Sinh}\left[\frac{2p_2 w}{R}\right]}\mathcal{G}\left(\sigma_A, \sigma_f^{(I;II)}, \tau_0\right), \quad (56)$$

$$B_2 = \frac{2\left(q_2\mathrm{Cosh}\left[\frac{p_2 w}{R}\right]\mathrm{Sin}\left[\frac{|q_2|w}{R}\right]-p_2\mathrm{Sinh}\left[\frac{p_2 w}{R}\right]\mathrm{Cos}\left[\frac{|q_2|w}{R}\right]\right)}{p_2\mathrm{Sin}\left[\frac{2|q_2|w}{R}\right]+q_2\mathrm{Sinh}\left[\frac{2p_2 w}{R}\right]}\mathcal{G}\left(\sigma_A, \sigma_f^{(I;II)}, \tau_0\right) - \frac{2\,\tau_0}{p_2\mathrm{Cosh}\left[\frac{p_2 w}{R}\right]\mathrm{Sin}\left[\frac{|q_2|w}{R}\right]+q_2\mathrm{Sinh}\left[\frac{p_2 w}{R}\right]\mathrm{Cos}\left[\frac{|q_2|w}{R}\right]}, \quad (57)$$

where

$$\mathcal{G}\left(\sigma_A, \sigma_f^{(I;II)}, \tau_0\right) = \sigma_A - \sigma_f^{(I;II)} + \frac{2\,\tau_0\,\mathrm{Sinh}\left[\frac{p_2 w}{R}\right]\mathrm{Sin}\left[\frac{|q_2|w}{R}\right]}{p_2\mathrm{Cosh}\left[\frac{p_2 w}{R}\right]\mathrm{Sin}\left[\frac{|q_2|w}{R}\right]+q_2\mathrm{Sinh}\left[\frac{p_2 w}{R}\right]\mathrm{Cos}\left[\frac{|q_2|w}{R}\right]}. \quad (58)$$

It should be noted that the coefficients A_2 and B_2 depend also on the radial displacement U_0 through the normal and shear stresses $\sigma_f^{(I;II)}$ and τ_0 which are coupled with U_0 (according to the displacement continuity conditions at the interface of parts (I) and (II) presented in the following). Since the yet unknown normal and shear stresses $\sigma_f^{(I;II)}$ and τ_0 and radial displacement U_0 depend on the applied axial, transverse and thermal loadings, the effects of applied loadings are also captured by the derived stress transfer function $D(z')$. For determination of the unknown stresses $\sigma_f^{(I;II)}$ and τ_0 and radial displacement U_0, the displacement continuity conditions at the interface of parts (I) and (II) in addition to the boundary condition for the applied transverse stress at the external surface will be utilized in the following. It is also worth noting that by applying boundary conditions (48) and (49) in part (I) and (54) and (55) in part (II), the boundary conditions (16) and (18) for continuity of the traction stresses at the interface of parts (I) and (II) in the fiber/fiber-image region ($0 \le r \le R$) are satisfied, that is:

$$\sigma_{zz}^{(I),f}(L) = \sigma_{z'z'}^{(II),fi}(w) = \sigma_f^{(I;II)}, \quad (59)$$

$$\sigma_{rz}^{(I),f}(r, L) = -\sigma_{rz'}^{(II),fi}(r, w) = \frac{\tau_0}{R} r. \quad (60)$$

Consequently, the boundary conditions (17) and (19) for continuity of the traction stresses at the interface of parts (I) and (II) in the matrix region ($R \le r \le a$) are automatically satisfied:

$$\sigma_{zz}^{(I),m}(L) = \sigma_{z'z'}^{(II),m}(w) = \frac{\sigma_A - S_f \sigma_f^{(I;II)}}{S_m}, \quad (61)$$

$$\sigma_{rz}^{(I),m}(r, L) = -\sigma_{rz'}^{(II),m}(r, w) = \frac{\tau_0}{S_m R}\left(\frac{R^2}{r} - S_f\, r\right). \quad (62)$$

The only yet unknown quantities to be determined are the circumferential radial displacement U_0, and the normal and shear stresses $\sigma_f^{(I;II)}$ and τ_0 identifying the stresses transferred across the interface between parts (I) and (II) (at $z = L$ and $z' = w$). Corresponding to the unknown radial displacement U_0, the boundary condition for the average transverse

stress at $r = a$ is used. For the unknown stresses $\sigma_f^{(I;II)}$ and τ_0 at the interface of parts (I) and (II), the axial and radial displacement continuity conditions are utilized correspondingly. For any given average transverse stress σ_T applied on the circumference of the cylindrical short fiber unit-cell, boundary condition (13) is rewritten as:

$$\int_0^L \sigma_{rr}^{(I),m}(a,z)\,dz + \int_0^w \sigma_{rr}^{(II),m}(a,z')\,dz' = (L+w)\sigma_T. \tag{63}$$

In order to have displacement continuity across the interface of parts (I) and (II), boundary conditions (20)-(23) should be satisfied. However, these boundary conditions can only be satisfied in the average sense. Therefore, continuity of the average axial and radial displacements at the interface of parts (I) and (II) is expressed by the following boundary conditions:

$$\bar{u}_z^{(I),m}(L) - \bar{u}_z^{(I),f}(L) = \bar{u}_{z'}^{(II),fi}(w) - \bar{u}_{z'}^{(II),m}(w), \tag{64}$$

$$S_f \bar{u}_r^{(I),f}(L) + S_m \bar{u}_r^{(I),m}(L) = S_f \bar{u}_r^{(II),fi}(w) + S_m \bar{u}_r^{(II),m}(w), \tag{65}$$

where Eqs. (41) and (42) are used to evaluate the average quantities over the fiber/fiber-image and matrix, respectively. In boundary conditions (63)-(65) the involved stress and displacement components corresponding to parts (I) and (II) can be obtained by using the derived solutions in Section 3. The three boundary conditions (63)-(65) are then solved simultaneously for the three unknowns U_0, $\sigma_f^{(I;II)}$ and τ_0 and therefore, each of these unknowns depend on the applied axial, transverse and thermal loadings as well as fiber/matrix properties. By obtaining these three unknowns and substituting into Eqs. (50), (51), (56) and (57), the coefficients A_1, B_1, A_2 and B_2 and hence the unique solutions for the stress transfer functions $C(z)$ and $D(z')$ corresponding to parts (I) and (II) are exactly identified. Therefore, the solution of the cylindrical short fiber system under any given axial, transverse and thermal loadings is analytically determined. It should be mentioned that the set of three boundary conditions (63)-(65) can still be solved for the three unknowns in a parametric form, but the solution will be too extensive. For this reason, it is much more convenient that for a given loading condition and fiber/matrix material properties, first the solutions of parts (I) and (II) are evaluated in terms of the three unknows (U_0, $\sigma_f^{(I;II)}$ and τ_0) and then the three boundary conditions (63)-(65) are solved for the three unknowns numerically.

5. Effective thermo-elastic properties of SFRCs

In this section, the analytical solutions for the cylindrical short fiber system developed in Sections 3 and 4 will be used for determination of the effective elastic properties of SFRCs. To this end, the behavior of the cylindrical short fiber model is examined under certain loading conditions. As the first loading condition, only axial stress σ_A is applied to the model while average transverse stress and temperature change are assumed to be zero. This loading condition is used for determination of the axial Young's modulus and axial Poisson's ratio of the composite. For the second loading condition,

the cylindrical system undergoes an average transverse stress σ_T while axial stress and temperature change are zero. By using this loading condition, the relationship between the transverse Young's modulus and transverse Poisson's ratio of the composite is obtained. Furthermore, the transverse shear modulus of the composite is estimated based on the Maxwell methodology and consequently, the transverse Young's modulus and Poisson's ratio of the composite are determined. The axial shear modulus of the composite is also estimated based on the Maxwell methodology and hence, the five independent effective constants of SFRCs with transverse isotropy are determined. Finally, the effective axial and transverse thermal expansion coefficients of the SFRC are determined by applying thermal loading while no axial and transverse stresses are applied to the cylindrical short fiber model.

For the axial loading condition, by letting $\sigma_T = \Delta T = 0$ the analytical closed-form solutions in both parts (I) and (II) can be obtained according to Sections 3 and 4 for any applied axial loading σ_A. The corresponding stress transfer functions $C(z)$ (Eq. (44)) and $D(z')$ (Eq. (47)) are then substituted into Eqs. (B.7) and (C.4), respectively for obtaining the functions $H_f^{(I)}(z) = H_m^{(I)}(z)$ and $H_f^{(II)}(z') = H_m^{(II)}(z')$. By substituting these functions into Eqs. (33) and (35) and using Eqs. (41) and (42) for evaluating the average axial displacements in both parts (I) and (II), the axial Young's modulus of the cylindrical short fiber composite model is obtained as

$$E_A^{eff} = \frac{\sigma_A}{\frac{\bar{u}_z^{(I),m}{}_{(L)} + \bar{u}_{z'}^{(II),m}{}_{(w)}}{L+w}} = \frac{\sigma_A}{\frac{\bar{u}_z^{(I),f}{}_{(L)} + \bar{u}_{z'}^{(II),fi}{}_{(w)}}{L+w}}, \tag{66}$$

noting that in Section 3, z' is defined as the axial coordinate in part (II) and therefore, the prime superscript over the variable z does not represent the derivative. In addition, by evaluating the circumferential radial displacement U_0 for this loading condition (Section 4), the axial Poisson's ratio for the cylindrical short fiber model can be given by

$$\nu_A^{eff} = -\frac{U_0 E_A^{eff}}{a \sigma_A}. \tag{67}$$

For the transverse loading condition, by letting $\sigma_A = \Delta T = 0$ the analytical closed-form solutions in both parts (I) and (II) can be obtained according to Sections 3 and 4 for any average transverse loading σ_T. Therefore, by evaluating the circumferential radial displacement U_0 for this loading condition, the relationship between the transverse Young's modulus (E_T^{eff}) and Poisson's ratio (ν_T^{eff}) of the cylindrical short fiber model can be obtained from the macroscopic radial or hoop strain component:

$$\frac{U_0}{a} = \frac{1-\nu_T^{eff}}{E_T^{eff}} \sigma_T. \tag{68}$$

In addition, for the transversely isotropic cylindrical short fiber model, the transverse Young's modulus and Poisson's ratio are related to the transverse shear modulus by:

$$\frac{E_T^{eff}}{2\left(1+\nu_T^{eff}\right)} = \mu_T^{eff}. \tag{69}$$

The transverse shear modulus is estimated by assuming uniform transverse shear strain for parts (I) and (II) under transverse shear stress. The validity of this assumption is assessed in Section 6 where the effective properties of SFRCs predicted by the current analytical model are compared with those of available data in the literature. Therefore, the effective transverse shear modulus of the cylindrical system is given by

$$\mu_T^{eff} = \frac{\mu_T^* L + \mu^m w}{L + w}, \tag{70}$$

where μ_T^{eff} is the effective transverse shear modulus of the cylindrical short fiber model, and μ_T^* is the transverse shear modulus of part (I) when it undergoes transverse shear stress separately. It can be shown that by using Maxwell methodology (see e.g., [18]), the transverse shear modulus of part (I) can be given by

$$\mu_T^* = S_f \mu_T^f + S_m \mu^m - \frac{\left(\mu_T^f - \mu^m\right)^2 S_f S_m}{S_m \mu_T^f + S_f \mu^m + \frac{\mu^m}{\kappa^m}}, \tag{71}$$

where κ^m is the Kolosov parameter corresponding to plane elasticity problems and generally represents plane strain or plane stress condition. However, the current problem under consideration is neither plane strain nor plane stress due to non-zero axial strain and non-zero axial stress, respectively. Therefore, when the cylindrical system of part (I) undergoes transverse loading the associated parameter κ^m can be obtained from the following equation in terms of the average axial, radial and circumferential stress components (over the whole length of part (I)):

$$\frac{3-\kappa^m}{4} = \frac{\nu^m}{1+\nu^m}\left(1 + \frac{\frac{1}{L}\int_0^L \bar{\sigma}_{zz}^{(I),m}(z)\, dz}{\frac{1}{L}\int_0^L \left[\bar{\sigma}_{rr}^{(I),m}(z) + \bar{\sigma}_{\theta\theta}^{(I),m}(z)\right] dz}\right). \tag{72}$$

It can be clearly seen that by letting $\bar{\sigma}_{zz}^{(I),m}(z) = 0$ in Eq. (72), one easily gets $\kappa^m = (3-\nu^m)/(1+\nu^m)$ which corresponds to the plane stress condition (zero axial stress). In contrast, assuming zero axial strain ($\epsilon_{zz}^m = 0$) readily gives $\bar{\sigma}_{zz}^{(I),m}(z) = \nu^m\left(\bar{\sigma}_{rr}^{(I),m}(z) + \bar{\sigma}_{\theta\theta}^{(I),m}(z)\right)$ and therefore, by substituting into Eq. (72) one easily gets $\kappa^m = 3 - 4\nu^m$ which corresponds to the plane strain condition (zero axial strain). Hence, by simultaneous solution of Eqs. (68) and (69), the transverse Young's modulus (E_T^{eff}) and Poisson's ratio (ν_T^{eff}) of the cylindrical short fiber model can be obtained as follows:

$$E_T^{eff} = \frac{4a\sigma_T \mu_T^{eff}}{a\sigma_T + 2U_0 \mu_T^{eff}}, \tag{73}$$

$$\nu_T^{eff} = \frac{a\sigma_T - 2U_0 \mu_T^{eff}}{a\sigma_T + 2U_0 \mu_T^{eff}}. \tag{74}$$

The axial shear modulus of the cylindrical model is estimated by assuming uniform axial shear strain for parts (I) and (II) under axial (anti-plane) shear stress. The validity of this assumption is assessed in Sections 6.2 and 6.4 where the effective axial shear modulus of SFRCs predicted by the current analytical model is compared with those available in the literature. Therefore, the effective axial shear modulus of the cylindrical system is given by

$$\mu_A^{eff} = \frac{\mu_A^* L + \mu^m w}{L+w}, \tag{75}$$

where μ_A^{eff} is the effective axial shear modulus of the cylindrical short fiber model, and μ_A^* is the axial shear modulus of part (I). By considering the 2D cross-section of the fiber-matrix double cylinder of part (I), it can be shown that the axial (anti-plane) shear modulus of part (I) can be given by (see e.g., [18, 61])

$$\mu_A^* = S_f \mu_A^f + S_m \mu^m - \frac{\left(\mu_A^f - \mu^m\right)^2 S_f S_m}{S_m \mu_A^f + (1+S_f)\mu^m}. \tag{76}$$

For the thermal loading condition, by letting $\sigma_A = \sigma_T = 0$ the analytical closed-form solutions in both parts (I) and (II) can be obtained according to Sections 3 and 4 for any applied thermal loading ΔT. The functions $H_f^{(I)}(z) = H_m^{(I)}(z)$ and $H_f^{(II)}(z') = H_m^{(II)}(z')$ are then substituted into Eqs. (33) and (35) and the axial displacements in the fiber/fiber-image and matrix are obtained. By using Eqs. (41) and (42) for evaluating the average axial displacements in both parts (I) and (II), the axial thermal expansion coefficient of the cylindrical short fiber composite model is obtained as

$$\alpha_A^{eff} = \frac{1}{\Delta T} \frac{\bar{u}_z^{(I),m}(L) + \bar{u}_{z'}^{(II),m}(w)}{L+w} = \frac{1}{\Delta T} \frac{\bar{u}_z^{(I),f}(L) + \bar{u}_{z'}^{(II),fi}(w)}{L+w}. \tag{77}$$

In addition, by evaluating the circumferential radial displacement U_0 for this loading condition (Section 4), the transverse thermal expansion coefficient of the cylindrical short fiber model can be determined:

$$\alpha_T^{eff} = \frac{U_0}{a\,\Delta T}. \tag{78}$$

In the next section, the effective axial and transverse thermo-elastic constants of Glass and Carbon SFRCs are evaluated by using the explained analytical formulations and moreover, accuracy and efficiency of the current model are verified by validating the predicted stress variations and effective thermo-elastic properties with available analytical and numerical data in the literature.

6. Results and discussion

In this section, the developed analytical model is used for determination of the effective thermo-elastic properties and stress transfers in SFRCs. To this end, in Section 6.1 variations of the stress components in the fiber and matrix of a SFRC are presented and compared with numerical and analytical results of the same cylindrical system available in the literature as well as two shear-lag models. The effective properties of Glass and Carbon SFRCs previously studied by numerical and analytical approaches in the literature are reexamined by the present analytical model in Section 6.2 and the efficiency and accuracy of the present theory are demonstrated. In Section 6.3 the effective axial moduli of Glass and Carbon SFRCs as well as their effective axial and transverse thermal expansion coefficients are predicted by the current model and these predictions are compared with those of an available enhanced MFH approach for the same fiber packing. In addition, in Section 6.3 by letting fibers' tip distances approach to zero, predictions of the current model are validated

with the limiting case of continuous fiber composites. Section 6.4 is devoted to prediction of the effective properties of a Glass/Polyamide SFRC and validating these predictions by those of an available enhanced MFH approach. At last, the effects of fiber aspect ratio on the effective axial modulus of Glass and Carbon SFRCs are studied in Section 6.5. It is worth noting that although the developed theory is valid for any desired fiber volume fraction, in this section SRFCs with volume fractions up to 20% are investigated since higher volume fractions in SFRCs are not frequently used.

6.1 Stress variations in a SFRC and comparison and validation with available data (Ref. [53])

In order to study the accuracy of the developed closed-form analytical solution, it would be beneficial to evaluate the variations of the stress fields by the current analytical model and compare the stress variations with those provided in the literature for the identical cylindrical model. In this section, variations of the stress components in a SFRC previously studied by Jiang et al. [53] are evaluated by the current analytical solution and compared with numerical and analytical results given in Ref. [53]. It should be noted that the analytical approach of Jiang et al. [53] basically differs from the currently developed analytical solution and therefore, predictions of these analytical models will be different. The numerical and analytical stress variations given in Ref. [53] also correspond to the cylindrical short fiber model with similar boundary conditions including uniform radial displacement on the external surface of the cylinder (as in Eq. (15)). The SFRC is composed of short fibers with aspect ratio of 10 and fiber area of S_f=10% while the length of fiber-image w (the length of part (II)) is equal to half the length of the fiber (Ref. [53]). The isotropic SiC whisker short fibers and Aluminum matrix have Young's moduli of 483 GPa and 74 GPa, Poisson's ratios of 0.17 and 0.3, and thermal expansion coefficients of 4.3×10^{-6} $^{\circ}C^{-1}$ and 23.0×10^{-6} $^{\circ}C^{-1}$, respectively (see Ref. [53]). The average axial stress σ_{zz}^{f} of the fiber/fiber-image is given in Ref. [53] for axial tensile loading of 500 MPa and temperature change of $\Delta T = -200$ $^{\circ}C$ using numerical FE analysis and analytical calculation.

In Fig. 3(a), variations of the axial stress of the fiber/fiber image under axial tensile loading of 500 MPa obtained from the current analytical solution are shown along the normalized axial position and compared with numerical and analytical results given in Ref. [53]. It can be observed that the current analytical solution accurately predicts the average axial stress both inside and outside the fiber. The axial stress variations obtained from the current analytical model as well as the analytical result of Ref. [53] are both in good agreement with the precise FE numerical results of Ref. [53], however the stress field of the current analytical solution shows slightly better agreement with numerical results especially near the fiber tip outside the fiber. In addition, the axial stress variations inside the fiber predicted by the two shear-lag models of Cox [48] and Clyne [49] are shown in Fig. 3(a). While Cox shear-lag model considers zero axial stress at fiber tip, Clyne's model assumes that the axial stress at fiber tip is equal to the average of the remote matrix stress and the peak fiber stress in the absence of fiber tip stress transfer. It can be observed that both of the shear-lag

models overestimate the mid-fiber axial stress and generally do not provide good predictions for the fiber's axial stress. The two shear-lag models result in considerably higher variations of axial stress especially at the middle of the fiber compared to the accurate analytical and numerical predictions. In Fig. 3(b), variations of the axial stress of the fiber/fiber image under temperature change of $\Delta T = -200$ ℃ obtained from the current analytical solution are shown along the normalized axial position and compared with numerical and analytical results given in Ref. [53]. As shown in Fig. 3(b), the current analytical solution gives accurate predictions for the average axial stress both inside and outside the fiber. The axial stress variations obtained from the current analytical model as well as the analytical results of Ref. [53] are both in good agreement with the precise FE numerical results of Ref. [53], but the stress field of the current analytical solution is quite closer to the numerical results especially at the middle of the fiber.

Fig. 3

Moreover, variations of the radial stress component under axial tensile loading of 500 MPa are evaluated by the present closed-form analytical solution and compared in Fig. 4 with the FE numerical results and analytical calculations of the same cylindrical model given in Ref. [53]. In Fig. 4(a), variations of the radial stress at the interface of the fiber/fiber-image and matrix ($r = R$) are demonstrated along the normalized axial position. It is observed that the stress variations of the current analytical solution show good agreement with FE numerical results of Ref. [53], while the analytical results of Ref. [53] do not provide good predictions for the radial stress component near the fiber tip. In Fig. 4(b), variations of the radial stress of the matrix at the external surface of the cylinder ($r = a$) are demonstrated along the normalized axial position. It can be observed that the stress variations of the current analytical solution show good agreement compared to FE numerical results of Ref. [53], but the analytical results of Ref. [53] show a significant jump at $z = L$ and do not provide good predictions for the radial stress near the interface of parts (I) and (II), i.e., at $0.9L < z < 1.1L$. In the analytical treatment of Ref. [53], it has been assumed that radial and circumferential stress components in the transient solution are equal on the outer radius of the fiber ($r = R$) along the whole length of the cylindrical system. This additional assumption can explain the significant jumps in radial and circumferential stresses of their analytical solution compared with FE numerical results, since around the fiber tip the radial and circumferential stresses have significant variations individually and are not necessarily equal on the outer radius of the fiber. Comparisons of the axial and radial stress components reveal that the current closed-form analytical solution can accurately predict the stress variations in both the fiber/fiber-image and matrix domains.

Fig. 4

6.2 Effective properties of Glass and Carbon SFRCs and validation with available data (Ref. [54])

The analytical treatment of Jiang et al. [53] discussed in Section 6.1 has been recently utilized by Huang et al. [54] for predicting the effective axial modulus of SFRCs. Huang et al. [54] obtained other effective properties of SFRCs from the classical bridging model by modifying the first diagonal component of the bridging tensor (corresponding to the axial direction) using the utilized analytical treatment. In this section, predictions of the present analytical solution are compared with the effective axial modulus and other effective elastic constants of Glass and Carbon SFRCs predicted by Huang et al. [54]. Therefore, Glass and Carbon short fibers with volume fraction of 20% and various aspect ratios are considered. The fibers' tip distance (fiber packing) is the same as that in Ref. [54] and equal to $w_{\text{tip}} = 2D_f$ for different aspect ratios as the examined fiber aspect ratios are larger than 4. The Glass SFRC is composed of isotropic matrix with Young's modulus $E^m = 3.35$ GPa and Poisson's ratio $\nu^m = 0.35$ reinforced with isotropic short Glass fibers with material constants $E^f = 74$ GPa and $\nu^f = 0.2$. The Carbon SFRC is composed of the same matrix but reinforced with transversely isotropic short Carbon fibers with axial Young's modulus $E_A^f = 230$ GPa, transverse Young's modulus $E_T^f = 15$ GPa, axial Poisson's ratio $\nu_A^f = 0.2$, axial shear modulus $\mu_A^f = 15$ GPa, and transverse shear modulus $\mu_T^f = 7$ GPa.

Variations of the effective axial moduli of Glass and Carbon SFRCs with fiber aspect ratio are demonstrated in Figs. 5(a) and 5(b), respectively, and these variations are compared with both analytical and FE numerical results given in Ref. [54]. Moreover, the axial moduli of Glass and Carbon continuous fiber composites obtained from the rule of mixture are also shown in Figs. 5(a) and 5(b). As shown in Fig. 5(a), the effective axial moduli of Glass SFRCs with different aspect ratios obtained from the present analytical solution are in very good agreement with FE numerical results of Ref. [54] while the analytical approach of Ref. [54] overestimates the effective axial modulus of Glass SFRCs. Interestingly, as shown in Fig. 5(b) it is observed that the effective axial moduli of Carbon SFRCs with different aspect ratios evaluated by the present analytical solution are again in very good agreement with FE numerical results of Ref. [54]. For Carbon SFRCs, the analytical approach of Ref. [54] results in a considerable overestimation of the effective axial modulus of the composite. This overestimation is around 5 GPa for aspect ratios in the range between 16 and 64 which is equivalent to around 24%, 18% and 14% overestimation for aspect ratios of 16, 32 and 64, respectively.

Fig. 5

Furthermore, comparison of other effective constants is also beneficial for validating the accuracy of the proposed model. For the aforementioned Glass and Carbon SFRCs with 20% volume fraction, the five independent effective elastic constants are evaluated for typical fiber aspect ratio of 64 using the current analytical solution. In Table 1, these effective constants are compared with those of FE analysis and bridging model given in Ref. [54]. It can be observed that compared

to the FE results of Ref. [54], the present analytical solution gives accurate predictions for the effective axial modulus while predictions of the bridging model are not in very good agreement with FE results especially for Carbon SFRCs. However, both the present analytical model and the bridging model of Ref. [54] give good predictions for the four other elastic constants. It should be noted that in Ref. [54] the FE model has a cubic geometry. Therefore, the difference of the cylindrical and cuboidal geometries (in transverse direction) in the current model and FE model of Ref. [54] can explain the small differences in transverse properties given in Table 1.

Table 1

6.3 Effective axial modulus of Glass and Carbon SFRCs and validation with available data (Ref. [24])

In this section, the effective axial moduli of Glass and Carbon SFRCs are predicted by the developed analytical model and compared with the predictions of an available enhanced mean-field homogenization approach previously developed by the authors, [24]. Therefore, Glass and Carbon short fibers with aspect ratio of 20 and volume fraction of 13% are considered (see [24]). This volume fraction corresponds to weight fraction of 25% for Glass fibers and 20% for Carbon fibers. The Glass SFRC is composed of isotropic matrix with Young's modulus $E^m = 2.1$ GPa and Poisson's ratio $\nu^m = 0.3$ reinforced with isotropic short Glass fibers with material constants $E^f = 72$ GPa and $\nu^f = 0.22$. The Carbon SFRC is composed of the same matrix but reinforced with transversely isotropic short Carbon fibers with axial Young's modulus $E_A^f = 230$ GPa, transverse Young's modulus $E_T^f = 15$ GPa, axial Poisson's ratio $\nu_A^f = 0.256$, transverse Poisson's ratio $\nu_T^f = 0.20$, axial shear modulus $\mu_A^f = 24$ GPa, and transverse shear modulus $\mu_T^f = 6.25$ GPa. For both of the cylindrical Glass and Carbon short fibers, the fiber diameter (D_f) is assumed to be 10 μm in order to show the effects of fiber/matrix stiffness contrast in Glass and Carbon SFRCs with same fiber lengths and diameters. For determination of the effective axial and transverse thermal expansion coefficients of the Glass and Carbon SFRCs, the thermal expansion coefficients of the matrix and Glass fibers are assumed as 55×10^{-6} °C^{-1} and 5×10^{-6} °C^{-1}, respectively while the axial and transverse thermal expansion coefficients of the Carbon fibers are assumed as 1.1×10^{-6} °C^{-1} and 22.1×10^{-6} °C^{-1}, respectively.

By assuming any tip distance ($w_{\text{tip}} = 2w$) for the short fibers, the effective axial moduli of the Glass and Carbon SFRCs as well as their effective thermal expansion coefficients are obtained by using the developed analytical solution. In Fig. 6(a) variations of the effective axial moduli of Glass and Carbon SFRCs versus fibers' tip distance are shown in logarithmic scale. Moreover, the effective axial moduli of the same Glass and Carbon SFRCs predicted by the enhanced MFH of Ref. [24] for the single-fiber model are also given in Fig. 6(a). The enhanced MFH approach of Ref. [24] is based on homogenization of cubic short fiber RVEs with PBCs incorporating fibers' interactions. It is noted that in Ref. [24], predictions of the enhanced MFH method have been shown to be in a very good agreement with FE simulations. It

should be noted that in Ref. [24] the single-fiber model has a cubic geometry with PBCs and therefore, in order to compare with the predictions of the current cylindrical model, the tip distance of the fibers (w_{tip}) is set to be equal in the two models. By setting equal tip distance for the fibers, tip-to-tip interactions of the short fibers can be captured by the current cylindrical model as well as the available enhanced MFH approach (Ref. [24]). It can be observed in Fig. 6(a) that predictions of the current analytical closed-form solution are in very good agreement with those of the enhanced MFH approach for both Glass and Carbon SFRCs. In addition, when fibers' tip distance approaches to zero, the effective axial modulus of the current model is validated with the limiting case of continuous fiber composite. This validation verifies that the current analytical model accurately accounts for fibers' tip-to-tip interactions such that the effective axial modulus increases by decreasing the tip distance (w_{tip}). The axial moduli of Glass and Carbon continuous fiber composites obtained from the rule of mixture have the values of 11.19 GPa and 31.73 GPa, respectively which are recovered by the present solution when w_{tip} vanishes. Fig.6(b) demonstrates the variations of the effective axial and transverse thermal expansion coefficients for both Glass and Carbon SFRCs versus fibers' tip distance in logarithmic scale which are evaluated by the present analytical model. The convergence of the effective thermal expansion coefficients to those of continuous fiber systems for vanishing w_{tip} is observed in Fig. 6(b) as well. For the limiting case of continuous fibers (vanishing w_{tip}), the effective axial thermal expansion coefficients of Glass and Carbon SFRCs obtained from the present analytical model are 13.34×10^{-6} °C^{-1} and 4.24×10^{-6} °C^{-1}, respectively which are in very good agreement with the values predicted by e.g. Schapery [62] for continuous fiber composites as 13.17×10^{-6} °C^{-1} and 4.20×10^{-6} °C^{-1}, respectively. The effective transverse thermal expansion coefficients for the Glass and Carbon SFRCs obtained from the present model by vanishing w_{tip} converge to 56.51×10^{-6} °C^{-1} and 62.32×10^{-6} °C^{-1}, respectively and are again in good agreement with predictions of Schapery [62] for Glass and Carbon continuous fiber composites which are 59.13×10^{-6} °C^{-1} and 63.86×10^{-6} °C^{-1}, respectively.

Fig. 6

6.4 Effective axial and transverse properties of a Glass SFRC and validation with available data (Ref. [24])

In this section, the effective axial and transverse properties of a Glass/Polyamide SFRC are predicted by the present analytical solution and validated with those predicted in Ref. [24]. The Glass/Polyamide composite is composed of short glass fibers with aspect ratio of 24, diameter of 10 μm, and volume fraction of 10%. The Young's moduli of Glass fibers and Polyamide matrix are 76 GPa and 3.1 GPa while their Poisson's ratios are 0.22 and 0.35, respectively (see Ref. [24]). In Table 2, the effective properties of the Glass/Polyamide SFRC predicted by the present cylindrical model as well as the enhanced MFH approach of Ref. [24] are presented. The predicted effective properties correspond to different tip

distance of the fibers. The effective axial and transverse Young's moduli and Poisson's ratios as well as the effective axial shear modulus obtained from the current cylindrical model show very good agreement with those of the enhanced MFH approach when the tip distance of the fibers is assumed to be identical in the two models. This comparison reveals that the current analytical model is able to capture the tip-to-tip interactions of the fibers accurately and the predicted effective axial modulus decreases by increasing the tip distance.

Table 2

6.5 Effects of fiber aspect ratio on the effective axial modulus of Glass and Carbon SFRCs

In this section, the effects of fiber aspect ratio on the effective axial modulus of Glass and Carbon SFRCs are examined. To this end, Glass and Carbon short fibers with volume fraction of 13% are considered; the material properties of the short fibers and matrix are given in Section 6.3. The effective axial moduli of Glass and Carbon SFRCs with different fiber aspect ratios are obtained by using the developed analytical solution when the tip distance of the fibers ($w_{\text{tip}} = 2w$) is assumed as $w_{\text{tip}} = 4D_f$ and $w_{\text{tip}} = 8D_f$. In Fig. 7, variations of the effective axial modulus of the Glass and Carbon SFRCs are demonstrated versus the fiber aspect ratio in the range of 10 and 4000 in logarithmic scale. In addition, the effective axial modulus of Glass and Carbon continuous fiber systems are also indicated in Fig. 7 as "rule of mixture". It can be observed that in both of the Glass and Carbon SFRCs, by increasing the fiber aspect ratio the effective axial modulus approaches the effective axial modulus of continuous fiber composite which provides further validation of the present analytical solution. As shown in Fig. 7, in Glass SFRC with $w_{\text{tip}} = 4D_f$ for fiber aspect ratio of 20 the composite reaches 60% of the axial modulus of Glass continuous fiber system, but in Carbon SFRC with $w_{\text{tip}} = 4D_f$ the composite reaches 60% of the axial modulus of Carbon continuous fiber system when the fiber aspect ratio is 80. By increasing the fiber aspect ratio, the effective axial modulus of Glass SFRC shows a faster approach to the axial modulus of the continuous fiber system compared to Carbon SFRCs. It should be noted that the current closed-form analytical model provides the solution in a split second and therefore, it is much more computationally efficient than numerical methods while providing accurate predictions.

Fig. 7

7. Conclusions

In this paper, novel analytical closed-form solutions for determination of the stress transfer as well as the effective axial and transverse thermo-elastic properties of SFRCs are developed. The PBCs in the axial direction and uniform

circumferential radial displacement representing PLBCs in transverse direction are implemented in the cylindrical short fiber model which may be subjected to axial and transverse stresses and thermal loading. The interactions among the short fibers are considered through the periodic boundary conditions. The closed-form expressions for the stress and displacement fields are derived for the fiber, fiber-image and matrix. In the developed analytical solution, all of the equilibrium equations, stress-strain constitutive relations and compatibility equations as well as the stress/displacement boundary conditions are satisfied exactly. The only simplifying assumption is that the axial stress σ_{zz} in both the fiber/fiber-image and matrix is assumed to be a function of the axial coordinate only. Subsequently, the axial constitutive equation and the boundary conditions on the continuity of the axial and radial displacement components at the interface of parts (I) and (II) are satisfied in the average sense.

The developed analytical treatment enabled accurate prediction of the stress transfers and effective axial and transverse thermo-elastic properties of SFRCs. By comparison with FE numerical results available in the literature, it is concluded that the present analytical model results in rather accurate predictions for the stress variations in both the fiber/fiber-image and the matrix. It is revealed that the current model accurately predicts the effective response of SFRCs with various fiber aspect ratios and fiber packings. Furthermore, predictions of the current model converge to the limiting case of a continuous fiber system when the fibers' tip distance vanishes.

The effective axial and transverse thermal expansion coefficients of Glass and Carbon SFRCs are predicted and compared by the corresponding continuous fiber system. It is demonstrated that the axial thermal expansion coefficient of Glass SFRC is higher than that of the Carbon SFRC with same fiber volume fraction and aspect ratio, while the transverse thermal expansion coefficient of Carbon SFRC is higher than that of the Glass SFRC. Moreover, the transverse thermal expansion coefficients of both Glass and Carbon SFRCs are considerably higher than their axial thermal expansion coefficients. In Glass/Polyamide SFRC with 10% volume fraction, the effective axial modulus is much more sensitive to the tip distance of the fibers compared to other effective constants. By examining the effects of fiber aspect ratio in both Glass and Carbon SFRCs, it is observed that in Glass and Carbon SFRCs with 13% volume fraction and the same fiber distances, when the fiber aspect ratio is 20 and 80, respectively, the composite reaches 60% of the axial modulus of the corresponding continuous fiber system.

In is concluded that the developed closed-form solutions provide accurate stress and displacement variations and effective thermo-elastic properties of SFRCs in a split second. Therefore, the developed analytical model is much more computationally efficient than numerical methods.

Acknowledgements

The authors acknowledge the financial support from EIT Raw Materials project "RELICARIO" under Grant Agreement No. 18239.

The work of M. Hajikazemi forms part of the research programme of DPI, project 812T17.

Declaration of competing interest

The authors declare that they have no known competing financial interests or personal relationships that could have appeared to influence the work reported in this paper.

References

[1] P. Singh and M. Kamal, "The effect of processing variables on microstructure of injection molded short fiber reinforced polypropylene composites," *Polymer composites,* vol. 10, no. 5, pp. 344-351, 1989.

[2] M. Gupta and K. Wang, "Fiber orientation and mechanical properties of short-fiber-reinforced injection-molded composites: Simulated and experimental results," *Polymer Composites,* vol. 14, no. 5, pp. 367-382, 1993.

[3] S.-Y. Fu, B. Lauke, E. Mäder, C.-Y. Yue, and X. Hu, "Tensile properties of short-glass-fiber-and short-carbon-fiber-reinforced polypropylene composites," *Composites Part A: Applied Science and Manufacturing,* vol. 31, no. 10, pp. 1117-1125, 2000.

[4] S. Kammoun, I. Doghri, L. Adam, G. Robert, and L. Delannay, "First pseudo-grain failure model for inelastic composites with misaligned short fibers," *Composites Part A: Applied Science and Manufacturing,* vol. 42, no. 12, pp. 1892-1902, 2011.

[5] K. Wu, L. Wan, H. Zhang, and D. Yang, "Numerical simulation of the injection molding process of short fiber composites by an integrated particle approach," *The International Journal of Advanced Manufacturing Technology,* vol. 97, no. 9, pp. 3479-3491, 2018.

[6] G. Yang, M. Park, and S.-J. Park, "Recent progresses of fabrication and characterization of fibers-reinforced composites: A review," *Composites Communications,* vol. 14, pp. 34-42, 2019.

[7] G. He, "Development of an elastothermoviscoplasticity damage model for injection molded short fiber reinforced thermoplastics with anisotropic damage evolutions," *Mechanics of Advanced Materials and Structures,* vol. 26, no. 22, pp. 1889-1901, 2019.

[8] J. Corum, R. Battiste, M. Ruggles, and W. Ren, "Durability-based design criteria for a chopped-glass-fiber automotive structural composite," *Composites science and technology,* vol. 61, no. 8, pp. 1083-1095, 2001.

[9] K. Friedrich and A. A. Almajid, "Manufacturing aspects of advanced polymer composites for automotive applications," *Applied Composite Materials,* vol. 20, no. 2, pp. 107-128, 2013.

[10] F. V. Ferreira, I. F. Pinheiro, S. F. de Souza, L. H. Mei, and L. M. Lona, "Polymer composites reinforced with natural fibers and nanocellulose in the automotive industry: a short review," *Journal of Composites Science,* vol. 3, no. 2, p. 51, 2019.

[11] H. Jariwala and P. Jain, "A review on mechanical behavior of natural fiber reinforced polymer composites and its applications," *Journal of Reinforced Plastics and Composites,* vol. 38, no. 10, pp. 441-453, 2019.

[12] V. Komarov, E. Kurkin, M. Spirina, and E. Kishov, "Estimation of weight efficiency of topologically optimal aerospace structures," in *2019 9th International Conference on Recent Advances in Space Technologies (RAST)*, 2019: IEEE, pp. 95-101.

[13] G. C. Jacob, J. M. Starbuck, J. F. Fellers, S. Simunovic, and R. G. Boeman, "Crashworthiness of various random chopped carbon fiber reinforced epoxy composite materials and their strain rate dependence," *Journal of Applied Polymer Science,* vol. 101, no. 3, pp. 1477-1486, 2006.

[14] M. Nciri, D. Notta-Cuvier, F. Lauro, F. Chaari, Y. Maalej, and B. Zouari, "Viscoelastic–viscoplastic model for short-fiber-reinforced composites with complex fiber orientation," *Mechanics of Advanced Materials and Structures,* vol. 26, no. 10, pp. 842-853, 2019.

[15] P. Anandakumar, M. V. Timmaraju, and R. Velmurugan, "Development of efficient short/continuous fiber thermoplastic composite automobile suspension upper control arm," *Materials Today: Proceedings,* vol. 39, pp. 1187-1191, 2021.

[16] J. Thomason, "The influence of fibre length and concentration on the properties of glass fibre reinforced polypropylene: 5. Injection moulded long and short fibre PP," *Composites Part A: Applied Science and Manufacturing,* vol. 33, no. 12, pp. 1641-1652, 2002.

[17] J. F. Rakow and A. M. Waas, "The effective isotropic moduli of random fibrous composites, platelet composites, and foamed solids," *Mechanics of Advanced Materials and Structures,* vol. 11, no. 2, pp. 151-173, 2004.

[18] L. McCartney, "Maxwell's far-field methodology predicting elastic properties of multiphase composites reinforced with aligned transversely isotropic spheroids," *Philosophical Magazine,* vol. 90, no. 31-32, pp. 4175-4207, 2010.

[19] N. G. Karsli and A. Aytac, "Tensile and thermomechanical properties of short carbon fiber reinforced polyamide 6 composites," *Composites Part B: Engineering,* vol. 51, pp. 270-275, 2013.

[20] S. K. Gulrez, M. A. Mohsin, and S. Al-Zahrani, "Studies on crystallization kinetics, microstructure and mechanical properties of different short carbon fiber reinforced polypropylene (SCF/PP) composites," *Journal of Polymer Research,* vol. 20, no. 10, pp. 1-9, 2013.

[21] S. Velumani, P. Navaneetha Krishnan, and S. Jayabal, "Mathematical modeling and optimization of mechanical properties of short coir fiber-reinforced vinyl ester composite using genetic algorithm method," *Mechanics of Advanced Materials and Structures,* vol. 21, no. 7, pp. 559-565, 2014.

[22] K. Babu, P. Mohite, and C. Upadhyay, "Development of an RVE and its stiffness predictions based on mathematical homogenization theory for short fibre composites," *International Journal of Solids and Structures,* vol. 130, pp. 80-104, 2018.

[23] W. Shu and I. Stanciulescu, "Multiscale homogenization method for the prediction of elastic properties of fiber-reinforced composites," *International Journal of Solids and Structures,* vol. 203, pp. 249-263, 2020.

[24] E. Rashidinejad, H. Ahmadi, M. Hajikazemi, and W. Van Paepegem, "Modeling of geometric configuration and fiber interactions in short fiber reinforced composites via new modified Eshelby tensors and enhanced mean-field homogenization," *Mechanics of Materials,* vol. 162, p. 104059, 2021.

[25] A. Bernasconi, F. Cosmi, and D. Dreossi, "Local anisotropy analysis of injection moulded fibre reinforced polymer composites," *Composites Science and Technology,* vol. 68, no. 12, pp. 2574-2581, 2008.

[26] D. Lee, "Local anisotropy analysis based on the Mori-Tanaka model for multiphase composites with fiber length and orientation distributions," *Composites Part B: Engineering,* vol. 148, pp. 227-234, 2018.

[27] C. Nony-Davadie, L. Peltier, Y. Chemisky, B. Surowiec, and F. Meraghni, "Mechanical characterization of anisotropy on a carbon fiber sheet molding compound composite under quasi-static and fatigue loading," *Journal of Composite Materials,* vol. 53, no. 11, pp. 1437-1457, 2019.

[28] A. Jain, Y. Abdin, W. Van Paepegem, I. Verpoest, and S. V. Lomov, "Effective anisotropic stiffness of inclusions with debonded interface for Eshelby-based models," *Composite Structures,* vol. 131, pp. 692-706, 2015.

[29] S.-Y. Fu and B. Lauke, "An analytical characterization of the anisotropy of the elastic modulus of misaligned short-fiber-reinforced polymers," *Composites Science and Technology,* vol. 58, no. 12, pp. 1961-1972, 1998.

[30] B. Lauke and S.-Y. Fu, "Strength anisotropy of misaligned short-fibre-reinforced polymers," *Composites Science and Technology,* vol. 59, no. 5, pp. 699-708, 1999.

[31] M. De Monte, E. Moosbrugger, and M. Quaresimin, "Influence of temperature and thickness on the off-axis behaviour of short glass fibre reinforced polyamide 6.6–Quasi-static loading," *Composites Part A: Applied Science and Manufacturing,* vol. 41, no. 7, pp. 859-871, 2010.

[32] S. Mortazavian and A. Fatemi, "Effects of fiber orientation and anisotropy on tensile strength and elastic modulus of short fiber reinforced polymer composites," *Composites part B: engineering,* vol. 72, pp. 116-129, 2015.

[33] H. Cai *et al.*, "An effective microscale approach for determining the anisotropy of polymer composites reinforced with randomly distributed short fibers," *Composite Structures,* vol. 240, p. 112087, 2020.

[34] S.-Y. Fu and B. Lauke, "Effects of fiber length and fiber orientation distributions on the tensile strength of short-fiber-reinforced polymers," *Composites Science and Technology,* vol. 56, no. 10, pp. 1179-1190, 1996.

[35] D. Dray, P. Gilormini, and G. Régnier, "Comparison of several closure approximations for evaluating the thermoelastic properties of an injection molded short-fiber composite," *Composites Science and Technology,* vol. 67, no. 7-8, pp. 1601-1610, 2007.

[36] K. J. Meyer, J. T. Hofmann, and D. G. Baird, "Prediction of short glass fiber orientation in the filling of an end-gated plaque," *Composites Part A: Applied Science and Manufacturing,* vol. 62, pp. 77-86, 2014.

[37] S. Kari, H. Berger, and U. Gabbert, "Numerical evaluation of effective material properties of randomly distributed short cylindrical fibre composites," *Computational materials science,* vol. 39, no. 1, pp. 198-204, 2007.

[38] J. Zhao, D.-X. Su, J.-m. Yi, G. Cheng, L.-S. Turng, and T. Osswald, "The effect of micromechanics models on mechanical property predictions for short fiber composites," *Composite Structures,* vol. 244, p. 112229, 2020.

[39] Y. Zhong *et al.*, "Elastic properties of injection molded short glass fiber reinforced thermoplastic composites," *Composite Structures,* vol. 254, p. 112850, 2020.

[40] C. L. Tucker III and E. Liang, "Stiffness predictions for unidirectional short-fiber composites: review and evaluation," *Composites science and technology,* vol. 59, no. 5, pp. 655-671, 1999.

[41] C. Naili, I. Doghri, T. Kanit, M. Sukiman, A. Aissa-Berraies, and A. Imad, "Short fiber reinforced composites: Unbiased full-field evaluation of various homogenization methods in elasticity," *Composites Science and Technology,* vol. 187, p. 107942, 2020.

[42] T. Mori and K. Tanaka, "Average stress in matrix and average elastic energy of materials with misfitting inclusions," *Acta metallurgica,* vol. 21, no. 5, pp. 571-574, 1973.

[43] Y. Benveniste, "A new approach to the application of Mori-Tanaka's theory in composite materials," *Mechanics of materials,* vol. 6, no. 2, pp. 147-157, 1987.

[44] O. Pierard, C. Friebel, and I. Doghri, "Mean-field homogenization of multi-phase thermo-elastic composites: a general framework and its validation," *Composites Science and Technology,* vol. 64, no. 10-11, pp. 1587-1603, 2004.

[45] I. Doghri, L. Brassart, L. Adam, and J.-S. Gérard, "A second-moment incremental formulation for the mean-field homogenization of elasto-plastic composites," *International Journal of Plasticity,* vol. 27, no. 3, pp. 352-371, 2011.

[46] A. Jain, S. V. Lomov, Y. Abdin, I. Verpoest, and W. Van Paepegem, "Pseudo-grain discretization and full Mori Tanaka formulation for random heterogeneous media: Predictive abilities for stresses in individual inclusions and the matrix," *Composites science and technology,* vol. 87, pp. 86-93, 2013.

[47] P. A. Hessman, F. Welschinger, K. Hornberger, and T. Böhlke, "On mean field homogenization schemes for short fiber reinforced composites: unified formulation, application and benchmark," *International Journal of Solids and Structures,* p. 111141, 2021.

[48] H. Cox, "The elasticity and strength of paper and other fibrous materials," *British journal of applied physics,* vol. 3, no. 3, p. 72, 1952.

[49] T. Clyne, "A simple development of the shear lag theory appropriate for composites with a relatively small modulus mismatch," *Materials Science and Engineering: A,* vol. 122, no. 2, pp. 183-192, 1989.

[50] A. A. Gusev, "Controlled accuracy finite element estimates for the effective stiffness of composites with spherical inclusions," *International journal of solids and structures,* vol. 80, pp. 227-236, 2016.

[51] E. Rashidinejad and H. Shodja, "On the exact nature of the coupled-fields of magneto-electro-elastic ellipsoidal inclusions with non-uniform eigenfields and general anisotropy," *Mechanics of Materials,* vol. 128, pp. 89-104, 2019.

[52] E. Rashidinejad and H. Shodja, "Novel theories on magneto-electro-elastic ellipsoidal multi-inclusions and inhomogeneities and associated impotent fields," *Mechanics of Materials,* vol. 143, p. 103201, 2020.

[53] Z. Jiang, X. Liu, G. Li, and J. Lian, "A new analytical model for three-dimensional elastic stress field distribution in short fibre composite," *Materials Science and Engineering: A,* vol. 366, no. 2, pp. 381-396, 2004.

[54] Z.-M. Huang, C.-C. Zhang, and Y.-D. Xue, "Stiffness prediction of short fiber reinforced composites," *International Journal of Mechanical Sciences,* vol. 161, p. 105068, 2019.

[55] H. Shodja and F. Roumi, "Overall behavior of composites with periodic multi-inhomogeneities," *Mechanics of Materials,* vol. 37, no. 2-3, pp. 343-353, 2005.

[56] E. Rashidinejad and A. A. Naderi, "Analytical study of electro-elastic fields in quantum nanostructure solar cells: the inter-nanostructure couplings and geometrical effects," *Acta Mechanica,* vol. 229, no. 7, pp. 3089-3106, 2018.

[57] E. Rashidinejad and H. Shoja, "Analytical solutions for electro-elastic fields of periodic quantum nanostructures within transversely isotropic piezoelectric media: studying the geometry effects," *Modares Mechanical Engineering,* vol. 15, no. 12, pp. 46-54, 2016.

[58] J. A. Nairn, "A variational mechanics analysis of the stresses around breaks in embedded fibers," *Mechanics of Materials,* vol. 13, no. 2, pp. 131-154, 1992.

[59] L. McCartney, "Analytical model for sliding interfaces associated with fibre fractures or matrix cracks," *Comp. Mater. Continua,* vol. 35, no. 3, pp. 183-227, 2013.

[60] S. G. Advani and C. L. Tucker III, "The use of tensors to describe and predict fiber orientation in short fiber composites," *Journal of rheology,* vol. 31, no. 8, pp. 751-784, 1987.

[61] Z. Hashin and B. W. Rosen, "The elastic moduli of fiber-reinforced materials," *Journal of Applied Mechanics,* vol. 31, no. 2, pp. 223-232, 1964.

[62] R. A. Schapery, "Thermal expansion coefficients of composite materials based on energy principles," *Journal of Composite materials,* vol. 2, no. 3, pp. 380-404, 1968.

Appendix A. Closed-form solution of concentric continuous fiber-matrix cylinders

Consider a continuous transversely isotropic fiber with radius R embedded in an isotropic cylindrical matrix with radius $a > R$ so that the fiber cross-sectional area is $S_f = R^2/a^2$ and the matrix cross-sectional area is $S_m = 1 - S_f$. For the concentric cylindrical ensemble subjected to axial stress σ_A, uniform transverse stress σ_{TC} and uniform temperature change ΔT, the stress components associated with the fiber ($0 \le r \le R$) and matrix ($R \le r \le a$) are as follows (see Ref. [59]):

$$\sigma_f = \sigma_{zz}^f = E_A^f\left(\epsilon_A - \alpha_A^f \Delta T\right) + 2\nu_A^f\left(\sigma_{TC} - \frac{S_m \phi}{R^2}\right), \tag{A.1}$$

$$\sigma_{rr}^f = \sigma_{\theta\theta}^f = \sigma_{TC} + \phi\left(\frac{1}{a^2} - \frac{1}{R^2}\right), \tag{A.2}$$

$$\sigma_m = \sigma_{zz}^m = E^m(\epsilon_A - \alpha^m \Delta T) + 2\nu^m\left(\sigma_{TC} + \frac{S_f \phi}{R^2}\right), \tag{A.3}$$

$$\sigma_{rr}^m = \sigma_{TC} + \phi\left(\frac{1}{a^2} - \frac{1}{r^2}\right), \tag{A.4}$$

$$\sigma_{\theta\theta}^m = \sigma_{TC} + \phi\left(\frac{1}{a^2} + \frac{1}{r^2}\right), \tag{A.5}$$

where

$$\phi = \frac{\left(\nu^m - \nu_A^f\right)\epsilon_A + \left(\alpha_T^f + \nu_A^f \alpha_A^f\right)\Delta T - \left(\alpha^m + \nu^m \alpha^m\right)\Delta T + \left(\frac{1-\nu_T^f}{E_T^f} - \frac{2\left(\nu_A^f\right)^2}{E_A^f} - \frac{(1-2\nu^m)(1+\nu^m)}{E^m}\right)\sigma_{TC}}{\frac{1}{2R^2}\left(\frac{1}{\mu^m} + 2S_f\frac{(1-2\nu^m)(1+\nu^m)}{E^m}\right) + \frac{S_m}{R^2}\left(\frac{1-\nu_T^f}{E_T^f} - \frac{2\left(\nu_A^f\right)^2}{E_A^f}\right)}, \tag{A.6}$$

$$\epsilon_A = \frac{1}{E_A}(\sigma_A - 2\nu_A \sigma_{TC} + E_A \alpha_A \Delta T), \tag{A.7}$$

$$E_A = S_f E_A^f + S_m E^m + 4\lambda\left(\nu^m - \nu_A^f\right)^2 S_f S_m, \tag{A.8}$$

$$\nu_A = S_f\nu_A^f + S_m\nu^m + 2\lambda\left(\frac{1-\nu_T^f}{E_T^f} - \frac{2\left(\nu_A^f\right)^2}{E_A^f} - \frac{(1-2\nu^m)(1+\nu^m)}{E^m}\right)\left(\nu^m - \nu_A^f\right)S_fS_m, \tag{A.9}$$

$$E_A\alpha_A = S_fE_A^f\alpha_A^f + S_mE^m\alpha^m + 4\lambda\left(\nu^m - \nu_A^f\right)\left(\alpha^m + \nu^m\alpha^m - \alpha_T^f - \nu_A^f\alpha_A^f\right)S_fS_m, \tag{A.10}$$

$$\lambda = \frac{1}{\frac{1}{\mu^m} + 2S_f\frac{(1-2\nu^m)(1+\nu^m)}{E^m} + 2S_m\left(\frac{1-\nu_T^f}{E_T^f} - \frac{2\left(\nu_A^f\right)^2}{E_A^f}\right)}. \tag{A.11}$$

In addition, the displacement components associated with the fiber and matrix are of the following forms:

$$u_z^f = u_z^m = \epsilon_A z, \tag{A.12}$$

$$u_r^f = A_f r, \tag{A.13}$$

$$u_r^m = A_m r + \frac{\phi}{2\mu^m r}, \tag{A.14}$$

$$u_\theta^f = u_\theta^m = 0, \tag{A.15}$$

where

$$A_f = -\nu_A^f\epsilon_A + \left(\alpha_T^f + \nu_A^f\alpha_A^f\right)\Delta T + \left(\frac{1-\nu_T^f}{E_T^f} - \frac{2\left(\nu_A^f\right)^2}{E_A^f}\right)\left(\sigma_{TC} - \frac{S_m\phi}{R^2}\right), \tag{A.16}$$

$$A_m = -\nu^m\epsilon_A + (\alpha^m + \nu^m\alpha^m)\Delta T + \frac{(1-2\nu^m)(1+\nu^m)}{E^m}\left(\sigma_{TC} + \frac{S_f\phi}{R^2}\right). \tag{A.17}$$

Appendix B. Closed-form expressions associated with the solution of part (I)

Corresponding to the analytical solution of part (I) presented in Section 3, the derived closed-form expressions of the functions $L_1(z)$ and $L_2(z)$ in Eqs. (37) and (38) are given by

$$L_1(z) = -\frac{2\mu^m\nu^m}{E^mS_m}C(z) - \frac{3(\nu^m-1)a^2 + \left(\nu_T^f-\nu^m\right)R^2S_f - \left(1+\nu_T^f+2\nu^m\right)R^2 + 4(1+\nu^m)R^2\mathrm{Log}\left[\frac{R}{a}\right]}{16S_m}C''(z) + \frac{2\mu^m}{S_f}A_m^{(I)} + \frac{1}{R^2}\phi^{(I)} - \frac{2\mu^ma}{R^2}U_0, \tag{B.1}$$

$$L_2(z) = -\left(\frac{\nu_A^f}{E_A^f} - \frac{\nu^m}{E^m}\right)C(z) - \left(\frac{(1-\nu^m)(3a^2+R^2)}{32\mu^m} - \frac{\left(1-\nu_T^f\right)R^2}{32\mu_T^f} + \frac{(1-\nu^m)a^2S_f\mathrm{Log}\left[\frac{R}{a}\right]}{8\mu^mS_m}\right)C''(z) - A_f^{(I)} - \frac{S_m}{S_f}A_m^{(I)} + \frac{a}{R^2}U_0. \tag{B.2}$$

After simultaneous solution of Eqs. (37) and (38) in terms of the above expressions for $L_1(z)$ and $L_2(z)$, the functions $R_f^{(I)}(z)$ and $R_m^{(I)}(z)$ can be derived explicitly as

$$R_f^{(I)}(z) = \frac{R^2\left(\left(-4+S_m\left(1+\nu_T^f\right)\right)\gamma + S_m\left(1-\left(\nu_T^f\right)^2\right)\beta - 4\gamma\mathrm{Log}[S_f/S_m]\right)}{16S_m\left(\gamma+\left(1-\nu_T^f\right)\beta\right)}C''(z) + \frac{E_T^f\left(\nu^m(1+\nu^m)S_fE_A^f - \nu_A^f\beta\right)}{E_A^f\left(\gamma+\left(1-\nu_T^f\right)\beta\right)}C(z) - \frac{E_T^f\beta}{\gamma+\left(1-\nu_T^f\right)\beta}A_f^{(I)}$$
$$- \frac{(1+\nu^m)E^mE_T^fS_m}{\gamma+\left(1-\nu_T^f\right)\beta}A_m^{(I)} + \frac{\gamma}{R^2\left(\gamma+\left(1-\nu_T^f\right)\beta\right)}\phi^{(I)} + \frac{2E^mE_T^f}{a\left(\gamma+\left(1-\nu_T^f\right)\beta\right)}U_0, \tag{B.3}$$

$$R_m^{(I)}(z) = -\frac{R^2(1+\nu^m)\left((4-S_m)\gamma + \left(2\beta + E^m\left(S_m^2(1+\nu^m) - 2S_m\nu^m\right)\right)\left(1-\nu_T^f\right) - 2(1+\nu^m)\left(E^m - E_T^f(1-\nu^m) - E^m\nu_T^f\right)S_f\mathrm{Log}[S_f]\right)}{16S_m\left(\gamma+\left(1-\nu_T^f\right)\beta\right)}C''(z)$$

$$+\frac{\left(\left(\nu^m E_A^f-\nu_A^f E^m\right)\gamma+\nu^m(1-\nu^m)\left(1-\nu_T^f\right)E_A^f E^m\right)S_f}{(1-\nu^m)E_A^f S_m\left(\gamma+\left(1-\nu_T^f\right)\beta\right)}C(z)-\frac{(1+\nu^m)E_T^f E^m S_f}{\gamma+\left(1-\nu_T^f\right)\beta}A_f^{(I)}-\frac{\left((1+\nu^m)E_T^f S_m+\left(1-\nu_T^f\right)E^m\right)E^m}{\gamma+\left(1-\nu_T^f\right)\beta}A_m^{(I)}$$

$$-\frac{(1+\nu^m)\left(1-\nu_T^f\right)E^m S_f}{R^2\left(\gamma+\left(1-\nu_T^f\right)\beta\right)}\phi^{(I)}+\frac{\left((1+\nu^m)E_T^f+\left(1-\nu_T^f\right)E^m\right)E^m}{a\left(\gamma+\left(1-\nu_T^f\right)\beta\right)}U_0, \tag{B.4}$$

in which

$$\gamma=(1-(\nu^m)^2)E_T^f S_m, \tag{B.5}$$

$$\beta=\left(2-S_m(1+\nu^m)\right)E^m. \tag{B.6}$$

Furthermore, the closed-form expression for the functions $H_f^{(I)}(z)=H_m^{(I)}(z)$ can be obtained as

$$H_f^{(I)}(z)=H_m^{(I)}(z)=\frac{\left(1-\nu_T^f\right)R^4}{32\ \frac{f}{T}}\left\{\frac{1+\nu_T^f}{3}-\frac{\left(-4+S_m\left(1+\nu_T^f\right)\right)\gamma+S_m\left(1-\left(\nu_T^f\right)^2\right)\beta-4\gamma\mathrm{Log}[S_f]/S_m}{2S_m\left(\gamma+\left(1-\nu_T^f\right)\beta\right)}\right\}C'''(z)+\frac{\nu_A^f R^2}{8E_A^f}\left\{\frac{E_A^f}{\nu_A^f\mu_A^f}-1+\nu_T^f-\right.$$

$$\left.\frac{\left(-4+S_m\left(1+\nu_T^f\right)\right)\gamma+S_m\left(1-\left(\nu_T^f\right)^2\right)\beta-4\gamma\mathrm{L}\quad[S_f]/S_m}{S_m\left(\gamma+\left(1-\nu_T^f\right)\beta\right)}-\frac{2\left(1-\nu_T^f\right)\left(\nu^m(1+\nu^m)S_f E_A^f-\nu_A^f\beta\right)}{\nu_A^f\left(\gamma+\left(1-\nu_T^f\right)\beta\right)}\right\}C'(z)-$$

$$\frac{1}{E_A^f}\left\{\frac{2\nu_A^f E_T^f\left(\nu^m(1+\nu^m)S_f E_A^f-\nu_A^f\beta\right)}{E_A^f\left(\gamma+\left(1-\nu_T^f\right)\beta\right)}+1\right\}\int_0^z C(\xi)\,d\xi+\frac{2\nu_A^f}{E_A^f}\left\{\frac{E_T^f\beta}{\gamma+\left(1-\nu_T^f\right)\beta}A_f^{(I)}+\frac{(1+\nu^m)E^m E_T^f S_m}{\gamma+\left(1-\nu_T^f\right)\beta}A_m^{(I)}-\right.$$

$$\left.\frac{\gamma}{R^2\left(\gamma+\left(1-\nu_T^f\right)\beta\right)}\phi^{(I)}-\frac{2E^m E_T^f}{a\left(\gamma+\left(1-\nu_T^f\right)\beta\right)}U_0\right\}z. \tag{B.7}$$

The explicit expressions for the coefficients of the non-homogeneous fourth-order differential equation (43) are derived as follows:

$$F^{(I)}=\frac{1}{192E^m E_T^f S_f S_m^2\left(\gamma+\left(1-\nu_T^f\right)\beta\right)}\left(7\gamma(1-\nu^m)\left(E^m\left(1-\nu_T^f\right)+E_T^f(1+\nu^m)\right)-S_f^3(1+\nu^m)(\omega-\gamma)\eta-S_f(1-\right.$$

$$\nu^m)\left(15E_T^f(1+\nu^m)\gamma-E^m\left(1-\nu_T^f\right)\omega-S_m E^m E_T^f(1+\nu^m)\left(1-\nu_T^f\right)\left(24+15\nu^m+\nu_T^f\right)\right)+S_f^2\left(\frac{9\gamma^2}{S_m}+\right.$$

$$2\nu^m\left(1-\nu_T^f\right)E^m\omega-\left(1-\nu_T^f\right)\left(9+9\nu^m+2\nu_T^f\right)E^m\gamma\Big)+12\gamma\frac{S_f\mathrm{Log}[S_f]}{S_m}\left(-\gamma+E^m\left(1-\nu_T^f\right)(2+S_m+\right.$$

$$\left.\left.\nu^m S_m)+2\eta(1+\nu^m)\mathrm{Log}\left[S_f\right]\right)\right), \tag{B.8}$$

$$G^{(I)}=\frac{1}{8E^m E_A^f\mu_A^f S_m^2\left(\gamma+\left(1-\nu_T^f\right)\beta\right)}\left(8\gamma S_f E^m\mu_A^f\nu_A^f+S_m S_f^2 E_A^f(1+\nu^m)\left(E^m-2\mu_A^f(1+\nu^m)\right)\eta+2S_f E_A^f\left(S_m E^m(1+\right.\right.$$

$$\nu^m)\left(E_T^f(1-\nu^m)+2\mu_A^f\left(1-\nu_T^f\right)\right)-4\gamma\mu_A^f(1+\nu^m)-\omega E^m\frac{\nu^m}{1+\nu_T^f}\Big)-8\gamma E^m\mu_A^f\nu_A^f-S_m E_A^f(1-\nu^m)\left(E^m-\right.$$

$$\left.6\mu_A^f(1+\nu^m)\right)\left(E^m\left(1-\nu_T^f\right)+E_T^f(1+\nu^m)\right)+2\mu_A^f(1+\nu^m)\mathrm{Log}\left[S_f\right]\left(\gamma E_A^f\left(2-S_f\nu^m\right)-2\gamma E^m\frac{\nu_A^f}{1+\nu^m}+\right.$$

$$E^m E_A^f\left(1-\nu_T^f\right)\left(2(1-\nu^m)-S_f^2\nu^m(1+\nu^m)+S_f((\nu^m)^2-\nu^m+2)\right)\Bigg)-2\mu_A^f\mathrm{Log}[S_f]\big(2\gamma E^m\nu_A^f+$$

$$\eta S_m S_f E_A^f\nu^m(1+\nu^m)^2\big)\Bigg), \tag{B.9}$$

$$H^{(I)}=\frac{1}{E^m\left(E_A^f\right)^2 S_m\left(\gamma+\left(1-\nu_T^f\right)\beta\right)}\Bigg(-2\beta S_m E^m E_T^f\left(\nu_A^f\right)^2+S_f\left(E_A^f\right)^2(1+\nu^m)\left(S_m E_T^f(1-\nu^m-2(\nu^m)^2)+E^m\big(1+S_f-$$

$$2\nu^m\big)\big(1-\nu_T^f\big)\big)+S_m E^m E_A^f\left(E_T^f(1+\nu^m)\big(S_m-\nu^m+S_f\nu^m+4S_f\nu^m\nu_A^f\big)+\big(1-\nu_T^f\big)\beta\right)\Bigg), \tag{B.10}$$

$$K^{(I)}=\frac{-1}{E^m E_A^f R^2\left(\gamma+\left(1-\nu_T^f\right)\beta\right)}\Bigg(2E^m E_T^f\left(\nu_A^f\beta-S_f E_A^f\nu^m(1+\nu^m)\right)A_f^{(I)}+2E^m\left(\frac{\nu_A^f E^m-\nu^m E_A^f}{1-\nu^m}\gamma-E^m E_A^f\nu^m\big(1-$$

$$\nu_T^f\big)\Bigg)A_m^{(I)}+\left(2\gamma S_f\left(\nu^m E_A^f-\nu_A^f E^m\right)+2S_f\nu^m E^m E_A^f\big(1-\nu_T^f\big)\big(S_f-2\nu^m+S_f\nu^m\big)+2\beta S_m\nu_A^f E^m\big(1-$$

$$\nu_T^f\big)\Big)\frac{\phi^{(I)}}{R^2}-2E^m\left(2E^m E_T^f\nu_A^f-E_A^f E_T^f\nu^m(1+\nu^m)-E^m E_A^f\nu^m\big(1-\nu_T^f\big)\right)\frac{U_0}{a}-2\big(\nu_A^f E^m-\nu^m E_A^f\big)\big(\gamma+\big(1-$$

$$\nu_T^f\big)\beta\big)\sigma_{TC}^{(I)}+E^m E_A^f\left(\alpha_A^f-\alpha^m\right)\big(\gamma+\big(1-\nu_T^f\big)\beta\big)\Delta T+E^m\big(\gamma+\big(1-\nu_T^f\big)\beta\big)\sigma_f^{(I)}-E_A^f\big(\gamma+\big(1-\nu_T^f\big)\beta\big)\sigma_m^{(I)}\Bigg), \tag{B.11}$$

with

$$\omega=\left(1-\left(\nu_T^f\right)^2\right)E^m S_m, \tag{B.12}$$

$$\eta=E^m\big(1-\nu_T^f\big)-E_T^f(1-\nu^m). \tag{B.13}$$

Appendix C. Closed-form expressions associated with the solution of part (II)

For determination of the analytical closed-form solution of part (II), first the unknown functions $R_f^{(II)}(z')$, $R_m^{(II)}(z')$, and $Y_m^{(II)}(z')$ are derived as

$$Y_m^{(II)}(z')=a^2\left(\frac{3(\nu^m-1)R^2}{16S_m}D''(z')+\frac{\nu^m S_f}{(1+\nu^m)S_m}D(z')-\frac{1-\nu^m}{1+\nu^m}R_m^{(II)}(z')-2\mu^m A_m^{(II)}\right)+2\mu^m a\,U_0, \tag{C.1}$$

$$R_f^{(II)}(z')=\frac{R^2(1+\nu^m)\left(S_f-1-2\mathrm{Log}[S_f]\right)}{16S_m}D''(z')-\frac{\nu^m}{2}D(z')-\frac{E^m}{1-\nu^m}A_m^{(II)}+\frac{E^m}{a(1-\nu^m)}U_0, \tag{C.2}$$

$$R_m^{(II)}(z')=\frac{R^2(1+\nu^m)(S_f-3)}{16S_m}D''(z')+\frac{\nu^m S_f}{2S_m}D(z')-\frac{E^m}{1-\nu^m}A_m^{(II)}+\frac{E^m}{a(1-\nu^m)}U_0, \tag{C.3}$$

noting that for part (II) we have $A_f^{(II)}=A_m^{(II)}$ and $\phi^{(II)}=0$ (see Appendix A). By rewriting Eq. (39) for part (II) and substituting Eqs. (24), (26), (27) and (33), the unknown functions $H_f^{(II)}(z')=H_m^{(II)}(z')$ are determined as

$$H_f^{(II)}(z')=H_m^{(II)}(z')=\frac{R^4(1-(\nu^m)^2)(5S_m+6\mathrm{Log}[S_f])}{192E^m S_m}D'''(z')+\frac{R^2(1+\nu^m)\left(S_m(2+\nu^m)+2\nu^m\mathrm{Log}[S_f]\right)}{8E^m S_m}D'(z')-$$

$$\frac{1-(\nu^m)^2}{E^m}\int_0^{z'}D(\xi)\,d\xi+\left(\frac{2\nu^m}{1-\nu^m}A_m^{(II)}-\frac{2\nu^m}{a(1-\nu^m)}U_0\right)z'. \tag{C.4}$$

The explicit expressions for the coefficients of the homogeneous fourth-order differential equation (46) are then obtained as follows:

$$F^{(II)} = \frac{(1-(\nu^m)^2)\left(7-2S_f-5S_f^2+12S_f\mathrm{Log}[S_f]\right)}{192E^m S_f S_m^2}, \tag{C.5}$$

$$G^{(II)} = \frac{(1-(\nu^m)^2)(S_m+\mathrm{Log}[S_f])}{2E^m S_m^2}, \tag{C.6}$$

$$H^{(II)} = \frac{1-(\nu^m)^2}{E^m S_m}. \tag{C.7}$$

Table 1. Effective elastic properties of Glass and Carbon SFRCs with 20% volume fraction and fiber aspect ratio of 64 predicted by the present analytical model and compared with predictions of FE analysis and bridging model given in Ref. [54].

		E_A^{eff}(GPa)	E_T^{eff}(GPa)	μ_A^{eff}(GPa)	μ_T^{eff}(GPa)	ν_A^{eff}
Glass SFRC	Present analytical model	15.822	5.013	1.806	1.710	0.312
	FE result in Ref. [54]	15.950	5.233	1.802	1.810	0.312
	Bridging model in Ref. [54]	16.922	5.326	1.802	1.800	0.322
Carbon SFRC	Present analytical model	34.988	4.675	1.750	1.603	0.319
	FE result in Ref. [54]	34.712	4.795	1.746	1.647	0.319
	Bridging model in Ref. [54]	39.308	4.806	1.747	1.630	0.327

Table 2. Effective elastic properties of Glass/Polyamide SFRC with 10% fiber volume fraction and fiber aspect ratio of 24 predicted by the present analytical model and the enhanced MFH approach in Ref. [24].

w_{tip} (μm)		E_A^{eff} (GPa)	E_T^{eff} (GPa)	μ_A^{eff} (GPa)	ν_A^{eff}	ν_T^{eff}
17	Present analytical model	8.67	3.89	1.39	0.33	0.45
	Enhanced MFH approach [24]	8.71	3.94	1.39	0.33	0.44
60	Present analytical model	7.79	3.88	1.39	0.33	0.44
	Enhanced MFH approach [24]	7.78	3.95	1.38	0.33	0.44
127	Present analytical model	6.88	3.88	1.39	0.32	0.44
	Enhanced MFH approach [24]	6.86	3.96	1.37	0.32	0.43

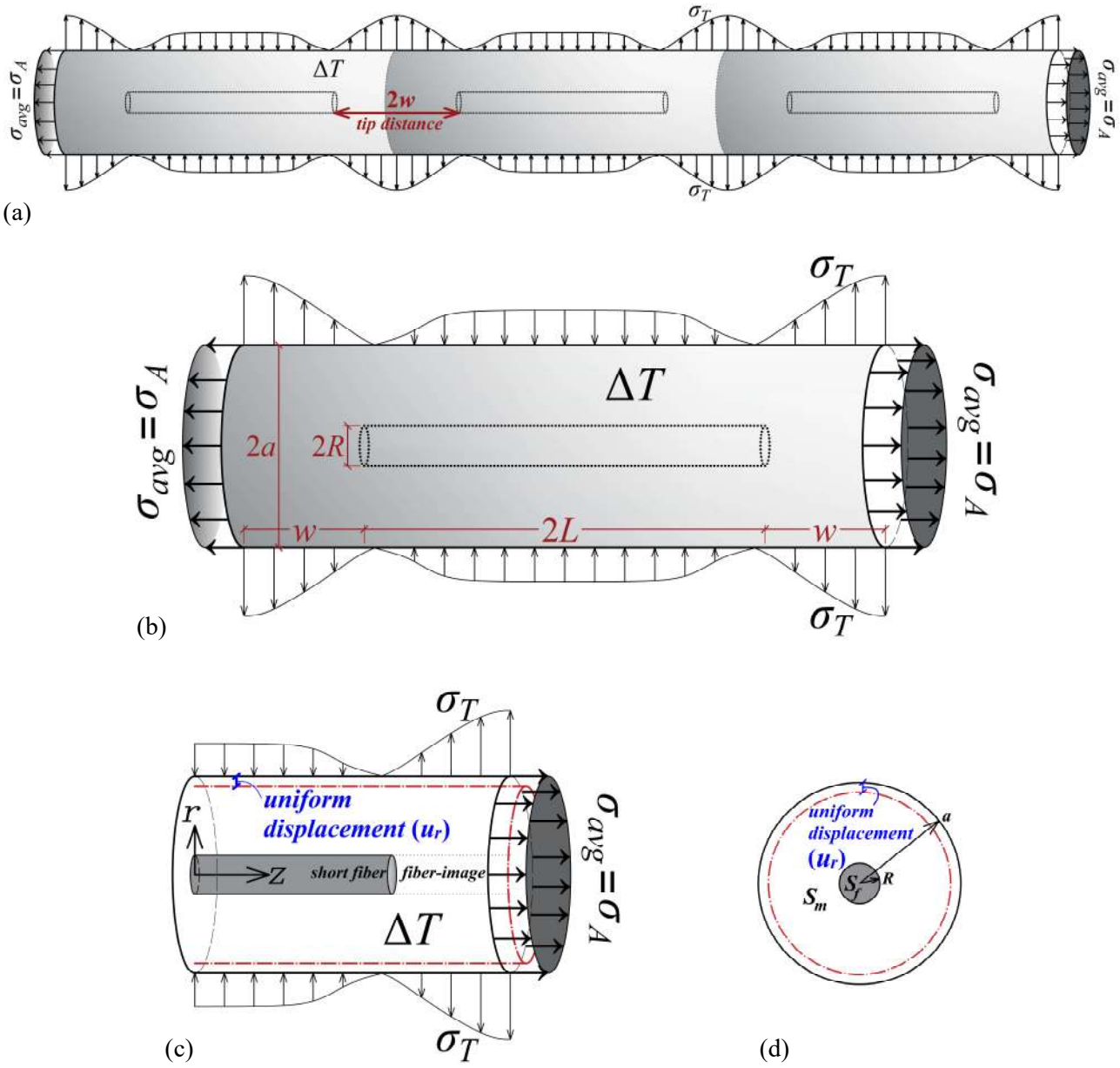

Fig.1. Cylindrical short fiber model subjected to average axial stress σ_A, average transverse stress σ_T, and uniform temperature change ΔT: (a) cylindrical ensemble with periodic boundary conditions (PBCs) in the axial direction, (b) geometrical characteristics of the cylindrical short fiber model, (c) uniform circumferential radial displacement representing periodic-like boundary conditions (PLBCs) in transverse direction, and (d) cross-section of the cylindrical ensemble showing fiber and matrix cross-sectional areas.

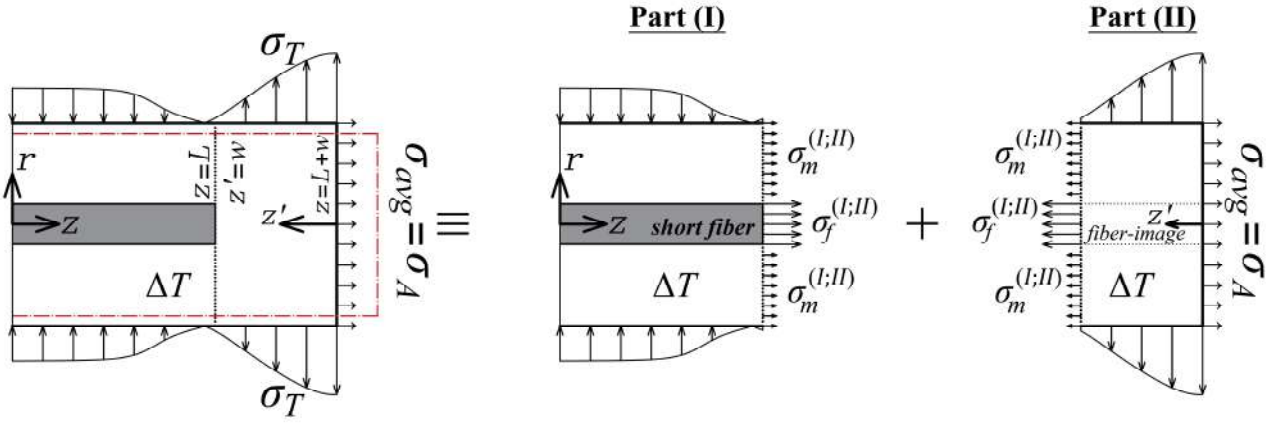

Fig. 2. Decomposition of the cylindrical short fiber model and associated stress components and cylindrical coordinates of parts (I) and (II).

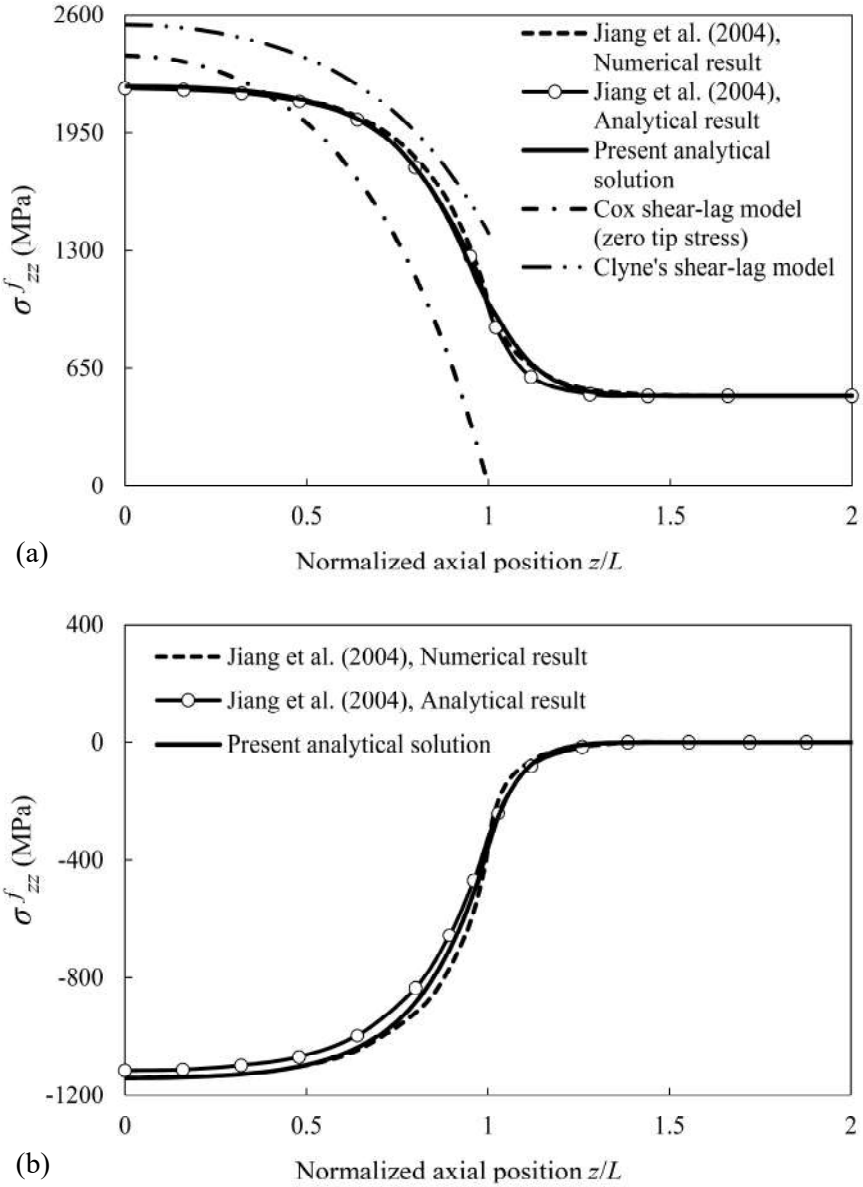

Fig. 3. Variations of the average axial stress in the fiber/fiber-image along the normalized axial position of the cylindrical short fiber system (with fiber-image length w equal to half the fiber length): (a) stress variations under axial tensile loading of 500 MPa obtained from the current analytical solution and compared with numerical and analytical results given by Jiang et al. [53] as well as shear-lag models of Cox [48] and Clyne [49], and (b) stress variations under temperature change of $\Delta T = -200$ ℃ obtained from the current analytical solution and compared with numerical and analytical results given by Jiang et al. [53].

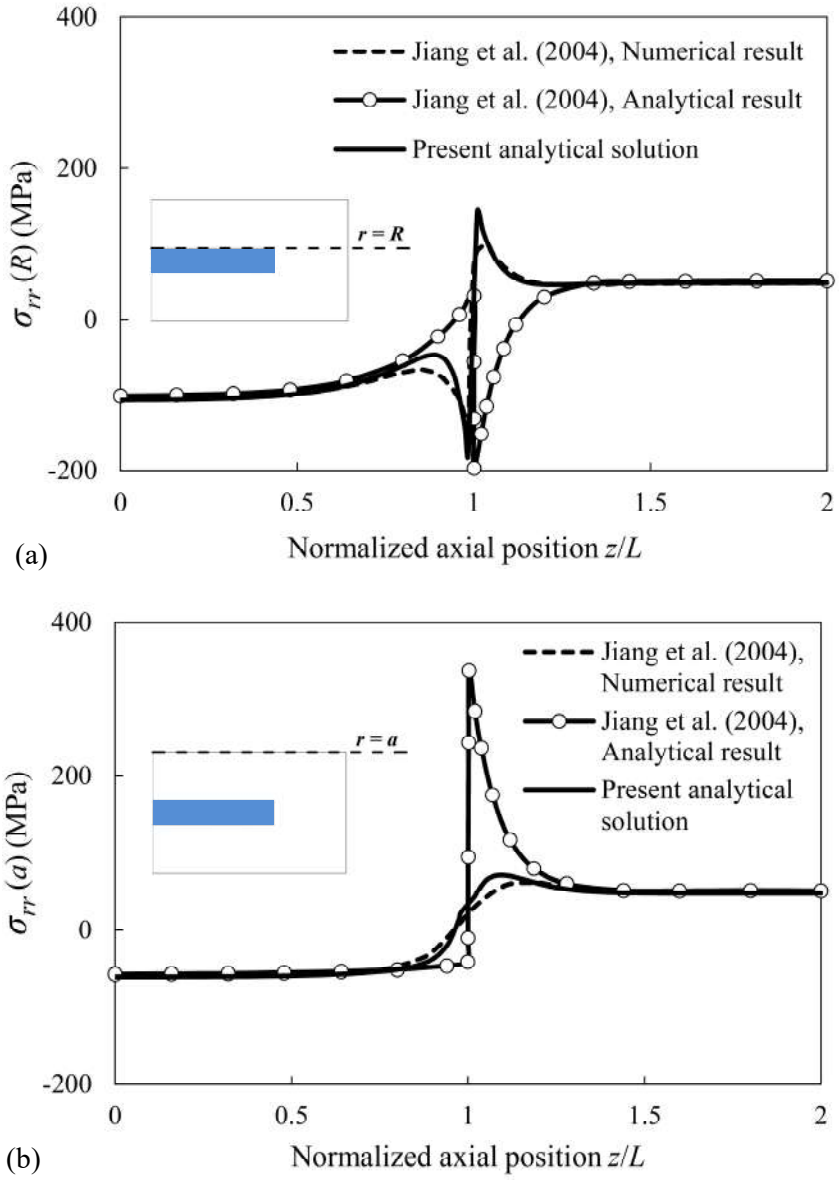

Fig. 4. Variations of the radial stress component along the normalized axial position for the cylindrical short fiber system (with fiber-image length w equal to half the fiber length) under axial tensile loading of 500 MPa obtained from the current analytical solution and compared with numerical and analytical results given by Jiang et al. [53]: (a) radial stress variations at the interface of the fiber/fiber-image and matrix ($r = R$), and (b) radial stress variations at the external surface of the cylinder ($r = a$).

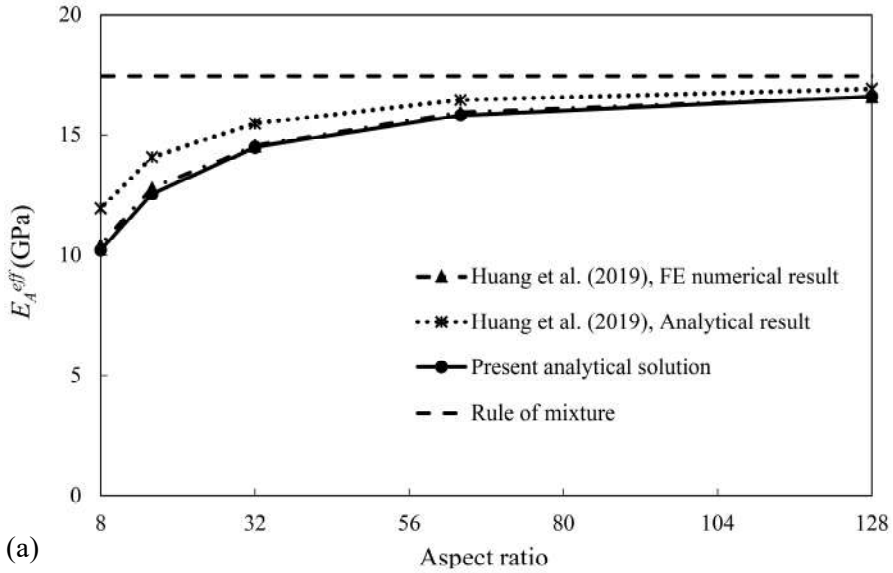

(a)

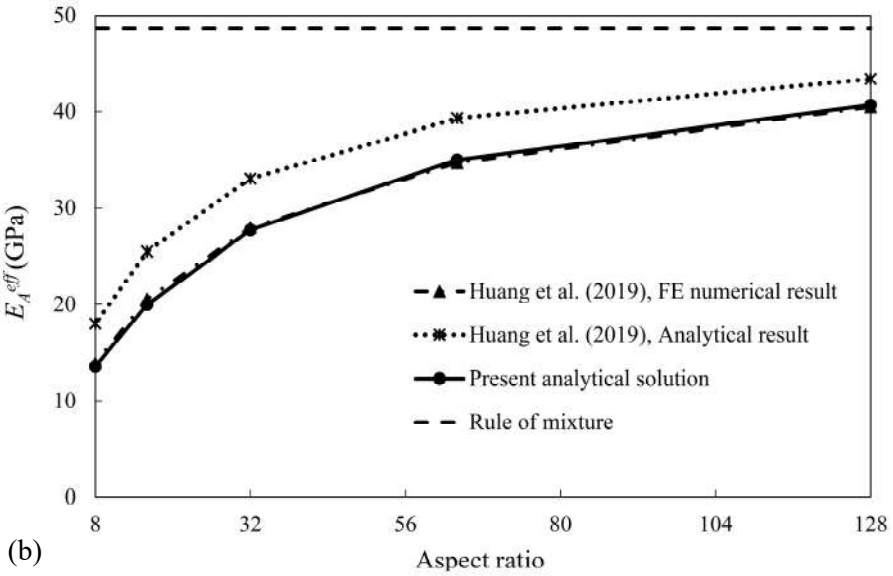

(b)

Fig. 5. Variations of the effective axial modulus of (a) Glass SFRC, and (b) Carbon SFRC, with 20% volume fraction versus fiber aspect ratio for the cylindrical short fiber system (with fiber-image length w equal to D_f) obtained from the current analytical solution and compared with analytical and FE numerical results given by Huang et al. [54]; the effective axial modulus of the corresponding continuous fiber system is indicated by the rule of mixture.

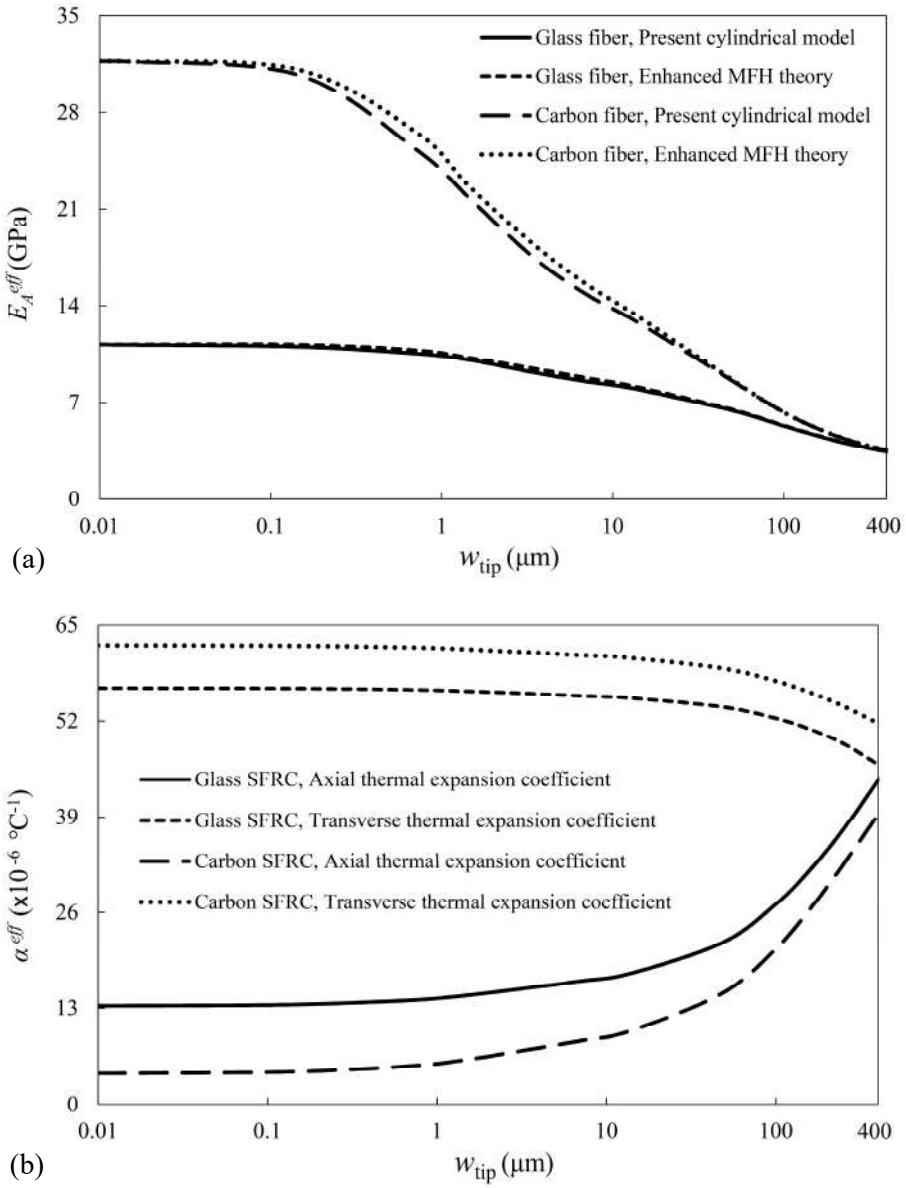

Fig. 6. Variations of the effective thermo-elastic properties of Glass and Carbon SFRCs with fiber aspect ratio of 20 and volume fraction of 13% versus fibers' tip distance in logarithmic scale: (a) variations of the effective axial modulus obtained from the present analytical solution for the cylindrical model compared to predictions of the enhanced MFH approach of Ref. [24], and (b) variation ns of the effective axial and transverse thermal expansion coefficients evaluated by the present analytical solution.

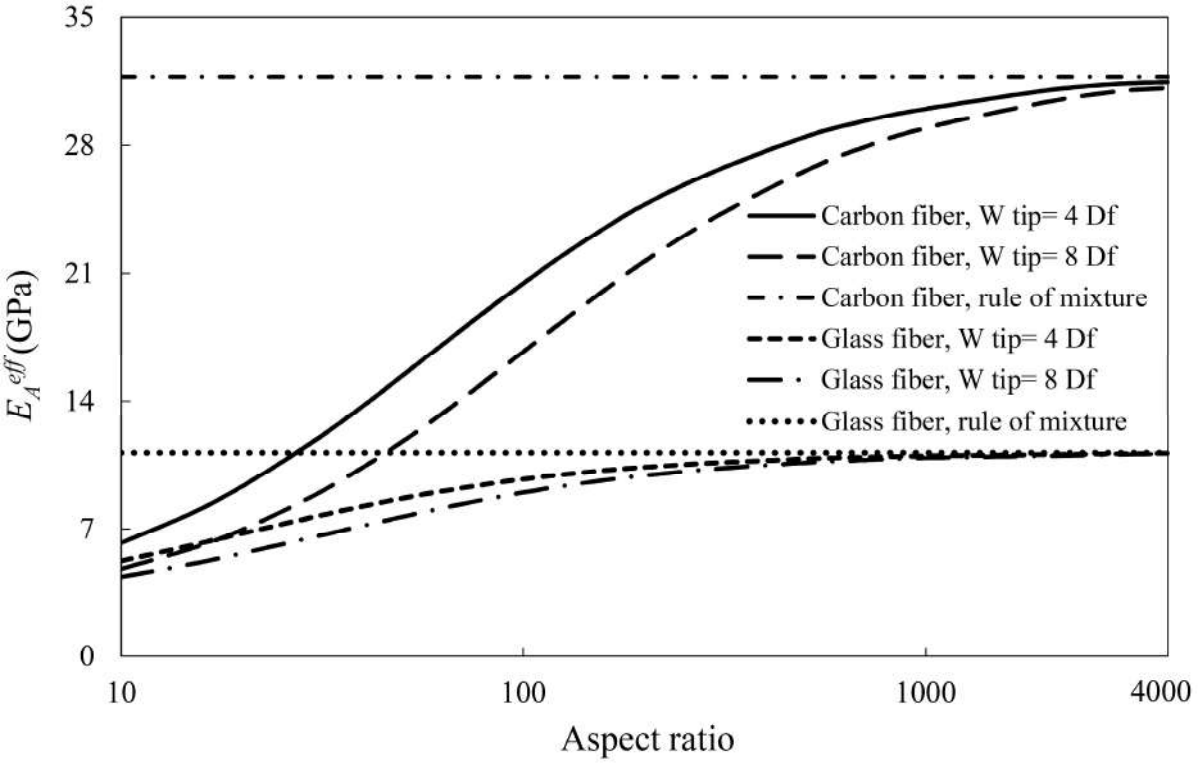

Fig. 7. Variations of the effective axial modulus of Glass and Carbon SFRCs with 13% volume fraction and different fibers' tip distances of $4D_f$ and $8D_f$ versus the fiber aspect ratio in logarithmic scale; the effective axial modulus of the corresponding continuous fiber system is indicated by the rule of mixture.

Figure captions

Fig.1. Cylindrical short fiber model subjected to average axial stress σ_A, average transverse stress σ_T, and uniform temperature change ΔT: (a) cylindrical ensemble with periodic boundary conditions (PBCs) in the axial direction, (b) geometrical characteristics of the cylindrical short fiber model, (c) uniform circumferential radial displacement representing periodic-like boundary conditions (PLBCs) in transverse direction, and (d) cross-section of the cylindrical ensemble showing fiber and matrix cross-sectional areas.

Fig. 2. Decomposition of the cylindrical short fiber model and associated stress components and cylindrical coordinates of parts (I) and (II).

Fig. 3. Variations of the average axial stress in the fiber/fiber-image along the normalized axial position of the cylindrical short fiber system (with fiber-image length w equal to half the fiber length): (a) stress variations under axial tensile loading of 500 MPa obtained from the current analytical solution and compared with numerical and analytical results given by Jiang et al. [53] as well as shear-lag models of Cox [48] and Clyne [49], and (b) stress variations under temperature change of $\Delta T = -200$ °C obtained from the current analytical solution and compared with numerical and analytical results given by Jiang et al. [53].

Fig. 4. Variations of the radial stress component along the normalized axial position for the cylindrical short fiber system (with fiber-image length w equal to half the fiber length) under axial tensile loading of 500 MPa obtained from the current analytical solution and compared with numerical and analytical results given by Jiang et al. [53]: (a) radial stress variations at the interface of the fiber/fiber-image and matrix ($r = R$), and (b) radial stress variations at the external surface of the cylinder ($r = a$).

Fig. 5. Variations of the effective axial modulus of (a) Glass SFRC, and (b) Carbon SFRC, with 20% volume fraction versus fiber aspect ratio for the cylindrical short fiber system (with fiber-image length w equal to D_f) obtained from the current analytical solution and compared with analytical and FE numerical results given by Huang et al. [54]; the effective axial modulus of the corresponding continuous fiber system is indicated by the rule of mixture.

Fig. 6. Variations of the effective thermo-elastic properties of Glass and Carbon SFRCs with fiber aspect ratio of 20 and volume fraction of 13% versus fibers' tip distance in logarithmic scale: (a) variations of the effective axial modulus obtained from the present analytical solution for the cylindrical model compared to predictions of the enhanced MFH approach of Ref. [24], and (b) variation ns of the effective axial and transverse thermal expansion coefficients evaluated by the present analytical solution.

Fig. 7. Variations of the effective axial modulus of Glass and Carbon SFRCs with 13% volume fraction and different fibers' tip distances of $4D_f$ and $8D_f$ versus the fiber aspect ratio in logarithmic scale; the effective axial modulus of the corresponding continuous fiber system is indicated by the rule of mixture.